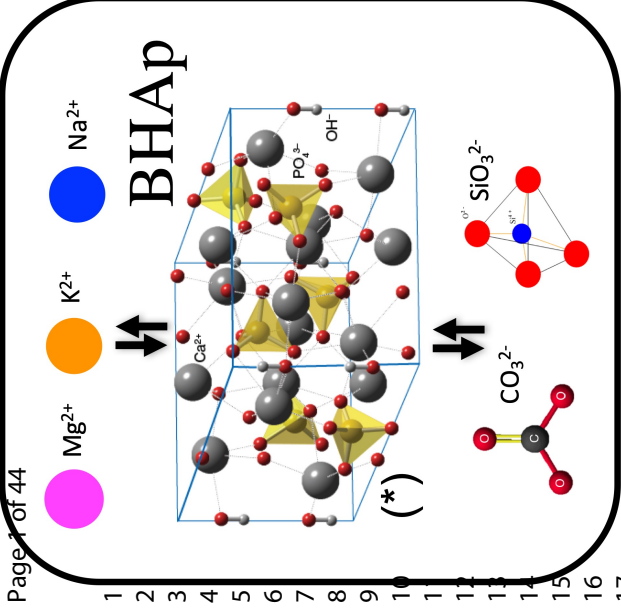


This document is confidential and is proprietary to the American Chemical Society and its authors. Do not copy or disclose without written permission. If you have received this item in error, notify the sender and delete all copies.

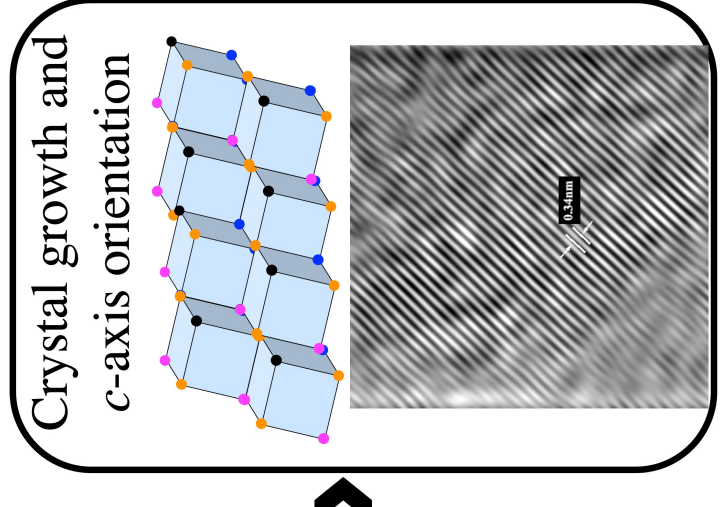
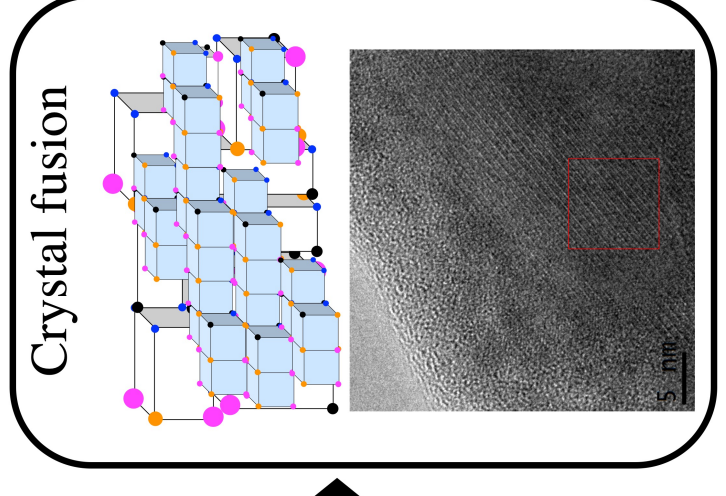
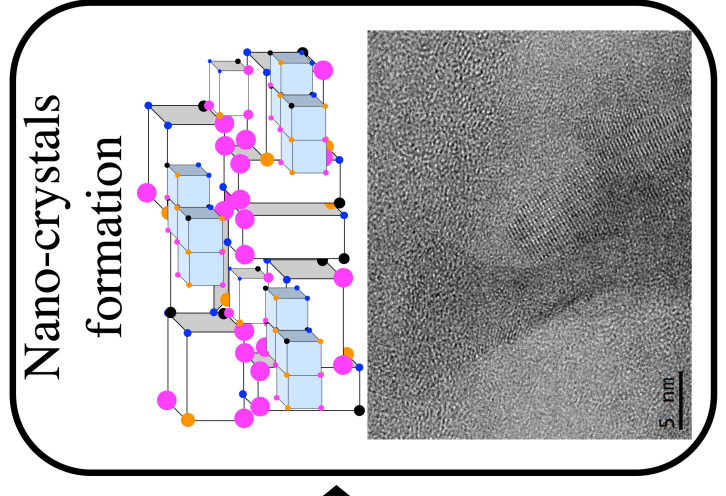
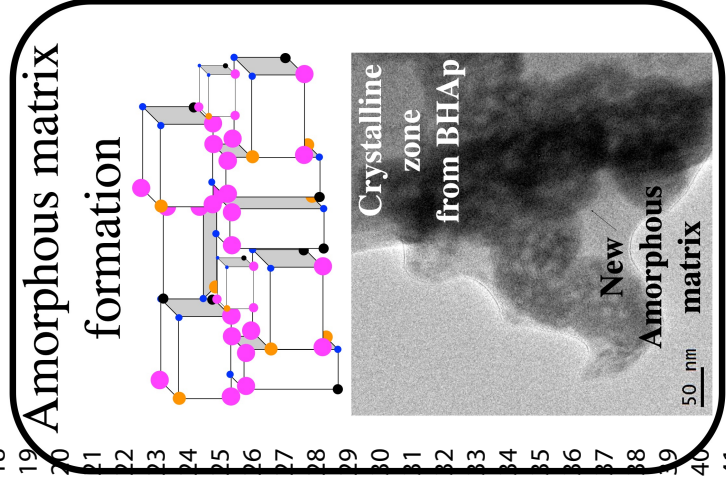
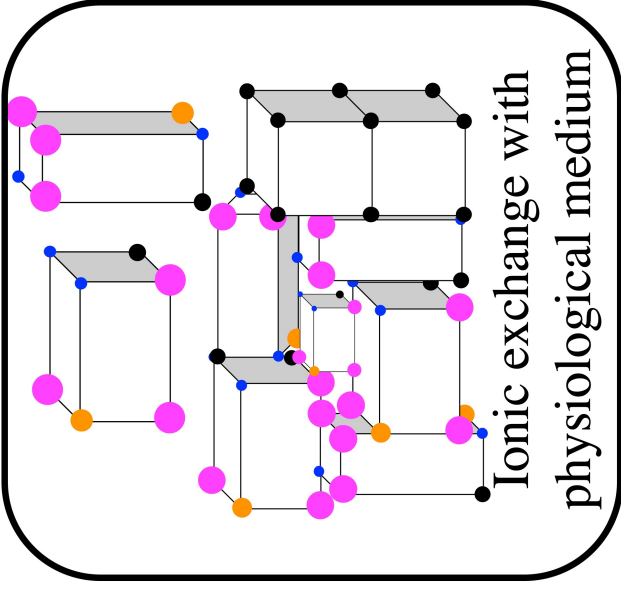
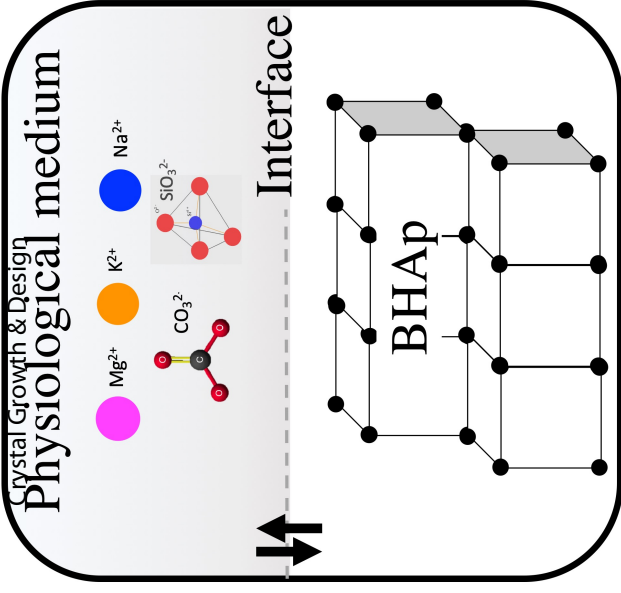
Preferred growth orientation of apatite crystals on biological hydroxyapatite enriched with bioactive glass: a biomimetic behavior

Journal:	<i>Crystal Growth & Design</i>
Manuscript ID	cg-2019-00268v.R1
Manuscript Type:	Article
Date Submitted by the Author:	n/a
Complete List of Authors:	Rincón López, July Andrea; CINVESTAV Queretaro, Materials Hermann, Jennifer; Centro de Investigación y de Estudios Avanzados Unidad Querétaro, Materials Science Cinca-Luis, Núria; Universitat de Barcelona, Centro de Proyección Térmica (CPT). Dpt. Ciència dels Materials i Química Física Garrido-Domiguez, Beatriz; Universitat de Barcelona, Centro de Proyección Térmica (CPT). Dpt. Ciència dels Materials i Química Física García-Cano, Irene; Universitat de Barcelona, Centro de Proyección Térmica (CPT). Dpt. Ciència dels Materials i Química Física Guilemany-Casadamon, Jose; Universitat de Barcelona, Centro de Proyección Térmica (CPT). Dpt. Ciència dels Materials i Química Física Alvarado-Orozco, Juan; Centro de Ingeniería y Desarrollo Industrial Muñoz-Saldaña, Juan; Centro de Investigación y de Estudios Avanzados Unidad Querétaro, Materials Science

SCHOLARONE™
Manuscripts



Biom mineralization process



Bone-like apatite recrystallization process



Preferred growth orientation of apatite crystals on biological hydroxyapatite enriched with bioactive glass: a biomimetic behavior

July Andrea Rincón-López ¹, Jennifer Andrea Hermann-Muñoz ¹, Núria Cinca-Luis ²,
Beatriz Garrido-Domiguez ², Irene García-Cano ², Jose Maria Guilemany-Casadamon ²,
Juan Manuel Alvarado-Orozco ^{3,4*}, Juan Muñoz-Saldaña ^{1*}

¹ Centro de Investigación y de Estudios Avanzados del IPN, Unidad Querétaro, Libramiento Norponiente #2000, Querétaro, Qro., C.P. 76230, México.

² Centro de Proyección Térmica (CPT). Dpt. Ciència dels Materials i Química Física, Universitat de Barcelona, c/Martí i Franquès 1, E-08028 Barcelona, Spain.

³ Centro de Ingeniería y Desarrollo Industrial, Av. Playa Pie de la Cuesta No. 702, Desarrollo San Pablo, Querétaro, Qro., C.P. 76125, México.

⁴ Consorcio de Manufactura Aditiva, CONMAD, Av. Pie de la Cuesta 702, Desarrollo San Pablo, Querétaro, México.

* Corresponding authors: jmunoz@cinvestav.mx, juan.alvarado@cidesi.edu.mx

Abstract

The morphological, structural and chemical transformations during the biomineralization process associated with the apatite formation from bovine-derived hydroxyapatite (BHAp) and BHAp/Nagelschmidite composite obtained from the mixture of BHAp and Vitryxx® bioactive glass are here presented. The study is focused on the structural characteristics of apatite formation and maturation process taking place at the biomaterial surface. The use of a biological HAp is of interest aiming to mimic the natural process of bone mineral matrix formation in the crystallization mechanism. This process was characterized by transmission electron microscopy (TEM), where the initial stage was identified as the formation of a hydrated amorphous matrix followed by the appearance of randomly oriented nanocrystals that later coalesce and grow with preferred orientation to *c*-axis. This behavior is a biomimetic process based on the alignment of natural bone apatite along collagen fibrils. The understanding of natural processes of mineral matrix formation at micro and nanoscale levels on bioactive materials is of great interest to address the effect of size, structure, and composition of apatite nanocrystals on the biologic phenomena involved in osseointegration.

Keywords: Biological hydroxyapatite, Nagelschmidite, apatite crystallization process, preferred orientation, transmission electron microscopy.

1. Introduction

Bioactive ceramics have the capability of bone bonding through the formation of bone-like apatite on its surface leading to an enhancement of bone tissue formation^{1,2}. This fact is tightly related to surface reactivity, which determines the biological performance of implanted materials^{2,3}. After implantation, several reactions take place at the biomaterial-tissue interface generating chemical, morphological and structural changes in the material and the surrounding tissue². The use of bioactive ceramics within the Ca-P-Si family such as Hydroxyapatite (HAp), Silicocarnotite (SC), Nagelschmidite (Nagel) and bioactive glasses (BG) for bone graft and tissue engineering purposes have attracted considerable attention in the last decades^{2,4-9}. A variety of materials and methods have been reported for the synthesis and processing of these bioactive ceramics, including the use of synthetic and biological sources, doping or adding ions to improve their biological responses and mechanical properties, among others^{6,7,10-13}. In the case of HAp, several studies have been carried out to increase its osteoconductive and osteoinductive properties and to mimic the behavior of natural apatites by the addition of CO_3^{2-} , SiO_4^{4-} , Mg^{2+} , Zn^{2+} , F^- , Cl^- , Sr^{2+} or Na^+ ions¹³⁻¹⁶. In some reports, HAp has been mixed with other bioactive materials such as BG to obtain either ceramic composites or bioactive phases⁸ able to release Si-containing ionic products which may stimulate the osteoblastic cells proliferation, differentiation, as well as the collagen I formation^{17,18}. Among biological hydroxyapatites, bovine derived-hydroxyapatite (BHAp) is a promising bioactive material due to its natural ionic substitutions. For instance, Na^+ ions increase the kinetic formation of apatite, facilitating the carbonation process and enhancing the osteoconductivity.

Moreover, Mg^{2+} ions stimulate the cellular adhesion to biomaterial surfaces and new bone formation^{19,20}. Previous results have shown that HAp doped with Mg^{2+} and Mg^{2+} together with CO_3^{2-} improved the behavior of MSC and MG-63 cells regarding adhesion, proliferation and metabolic activation compared to the stoichiometric one¹³. On the other hand, the economic and environmental implications of HAp extracted from biological source have increased its use for bone graft, as well as for coatings of metallic implants, among other biomedical applications²¹⁻²³.

The bioactivity of glass ceramics and ceramics such as HAp has been widely studied²⁴⁻²⁸. Many efforts have been focused on relating apatite-forming ability of biomaterials evaluated in solutions that simulate body fluid to their *in vivo* bioactivity and biocompatibility^{29,30}. The

1
2 general mechanism for bone-like apatite formation considers a cation exchange of the
3 bioactive material with protons from the body fluid, followed by the formation of an
4 amorphous calcium layer that crystallizes on a Ca-deficient apatite with compositional and
5 structural characteristics of bone mineral^{31,32}.
6
7

8
9 The growth kinetics of the bone-like apatite layer is assumed to be affected by the presence
10 of specific ions (*e.g.*, CO_3^{2-} , SiO_4^{4-} , Mg^{2+} , F^- , Cl^- , Na^+). For instance, the presence of SiO_4^{4-} ,
11 SiO_2 , silica-based glasses and Si-doped HAp accelerates the process of biomineralization
12 through the formation of Si-OH groups on its surface, which induces crystalline apatite
13 formation from either an amorphous calcium silicate or an amorphous calcium phosphate
14 (ACP)³³. On the other hand, it has been reported that the presence of P_2O_5 in sol-gel prepared
15 glass can promote the crystal growth of the apatite³⁴.
16
17

18
19 Since the process of bone-like apatite formation involves several microstructural changes,
20 conventional characterization techniques for the bioactivity evaluation include scanning
21 electron microscopy (SEM), X-ray diffraction (XRD) and Raman or infrared spectroscopies
22 ^{24,29}. However, the identification of the first stages of crystallization by XRD is challenging,
23 mainly due to the weak peak intensities generated by small precipitates volume. Further on,
24 the diffraction peaks of the substrates difficult the identification of apatite micro-crystals
25 formed on the bioactive surface³⁵.
26
27

28
29 Multiple studies related to bioactivity and chemical interactions occurring when a bioactive
30 material is immersed in simulated body fluid are available in the literature^{24,25,29–31,33,36}.
31 However, structural transformations and apatite layer crystallization taking place during the
32 biomineralization process have been scarcely reported. Current efforts to better understand
33 the apatite formation include diverse transmission electron microscopy (TEM) techniques,
34 such as High-Resolution TEM (HR-TEM), selected area electron diffraction (SAED)
35 patterns, Fourier Fast Transform (FFT), Inverse FFT (IFFT), cryoTEM, among others^{33,36–}
36 ⁴¹. In contrast to conventional XRD analysis, a TEM techniques offer the potential to
37 investigate the apatite formation mechanisms at the micro- and nano-scale levels to further
38 identify the maturation process, which starts with individual nanocrystals, crystal fusion and
39 finalizes with preferred orientation crystal growth^{35,38,42,43}.
40
41

42
43 This work reports on the morphological, structural and chemical transformations during the
44 biomineralization process of BHAp and BHAp/Nagel composite obtained from the mixture
45 of BHAp and Vitryxx® bioactive glass. Here, not only the use of a biological HAp respective
46
47
48
49
50
51
52
53
54
55
56
57
58
59
60

1
2 to the stoichiometric one and the effect of the bioactive glass enrichment is of interest, but
3
4 also a particular emphasis is given on the use of TEM techniques to elucidate the mechanism
5
6 of the bone-like apatite formation as well as further understanding of its growth kinetics.
7
8
9

10 **2. Material and methods**

11 **2.1. Sample preparation**

12
13 BHAp (Cinvestav, México)⁷ and Bioactive glass (Vitryxx®, Germany)⁴⁴ powders were used
14
15 to prepare dense ceramics following the preparation and characterization methodology
16
17 reported in a previous group contribution⁸. In a short description, the compositions studied
18
19 in this work were BHAp and 96.25%BHAp+3.75%BG (vol. %), corresponding to the first
20
21 two points from the systematic study performed on HAp/BG mixtures from 0 to 30 vol. %,
22
23 in steps of 3.75%, by mixtures design using Minitab®. The 96.25%BHAp+3.75%BG sample
24
25 leads exclusive to the formation of BHAp/Nagel composite (32.7 wt.% Nagel)⁸. For the
26
27 preparation of ceramics, the powders were milled, followed by a pressing step to form
28
29 ceramics in disk-shaped green samples previous to a sintering process at 1220 °C during 4 h
30
31 in lab air.

32 **2.2. Bioactivity and degradation assessment**

33
34 The in-vitro biomineralization process on the ceramic samples was studied using the
35
36 simulated body fluid H8264 (Sigma-Aldrich, Germany), *i.e.*, balanced salt Hank's solution
37
38 modified with sodium bicarbonate, without phenol red, sterile filtered and suitable for cell
39
40 culture. The ceramic composite's ability to form apatite after immersion in Hank's solution
41
42 was evaluated following the ISO/FDIS 23317: 2007(E) standard for ceramics and powders
43
44 samples⁴⁵. Sintered ceramics were immersed in 25 mL of Hank's solution and exposed for
45
46 0, 6, 14 and 28 days at 37 °C. The solution was changed every 3 days to avoid ionic saturation
47
48 of the medium and sample surface. Before and after immersion, sintered ceramics were
49
50 characterized using XRD, Raman spectroscopy and SEM/EDX to track the structural,
51
52 chemical and morphological changes on ceramics and powders surface related to the bone-
53
54 like apatite formation. TEM/EDX characterization was carried out on sintered BHAp and
55
56 BHAp/Nagel composite powders to analyze different stages of local transformation of
57
58 crystalline phases into apatite.

59
60 The degradation test was performed based on ISO 10993 standard, Part 14: "*Identification*

1
2 *and quantification of degradation products of ceramic materials*"⁴⁶, in which the pH found
3 on *in vivo* conditions is simulated. The material was exposed in granulated form to a buffer
4 solution of TRIS (hydroxymethyl aminomethane) with HCl, pH of 7.4 at 37 °C ± 1°C for
5 120 ± 1 h. After the exposure time, the precipitated particles were filtered and dried at 37 °C
6 during 24 h. The ionic concentrations of the resulting solution were measured using an
7 Inductively Coupled Plasma Optical Emission Spectrometer (ICP-OES, Optima 8300, Perkin
8 Elmer) to determine the leaching products of the samples are within acceptable limits
9 reported in the literature and its effect on the apatite formation.
10
11
12
13
14
15
16
17

18 **2.3. Sample characterization**

19 **2.3.1. SEM**

20
21
22
23 Microstructural characterization of sintered ceramics was performed before and after Hank's
24 solution exposure using a Scanning Electron Microscope JSM-7610F (JEOL) at 1 kV
25 electron acceleration voltage and a secondary electron (SE) detector. Samples were sputter-
26 coated with a gold-palladium thin layer to make the ceramic surface conductive. Moreover,
27 the chemical composition of sintered ceramics was measured using an EDX analyzer
28 (Bruker) coupled to the SEM. Grain size was then quantified following the ASTM E112
29 standard (*i.e.*, linear intercept method) from four micrographs recorded at different
30 magnifications (500 – 2500 X). The cross-section analysis was performed on fresh fractured
31 ceramics, a 10 kV electron acceleration voltage and a backscattering electron detector were
32 used to evaluate the thickness of the apatite layer.
33
34
35
36
37
38
39
40
41
42

43 **2.3.2. GXRD Characterization**

44
45 Structural characterization was performed on dense ceramics surface by grazing angle X-ray
46 diffraction (GXRD) with monochromatic CuK α radiation ($\lambda = 1.5406 \text{ \AA}$) operating at 30 kV
47 and 20 mA using a Siemens D-500 diffractometer. The XRD patterns were recorded from 10
48 to 70 ° on a 2 θ scale in steps of 0.02 ° intervals with a counting time of 2 s at each step.
49 Structural changes, after different immersion periods (0, 6, 14 and 28 days) in Hank's
50 solution, were measured at a grazing incidence angle of 1° on the ceramics surface. Rietveld
51 analysis of the XRD patterns was performed using GSAS[®] to characterize and quantify the
52 phase fraction in each sample, as well as to determine the crystallographic parameters of the
53
54
55
56
57
58
59
60

growing bone-like apatite according to the process and analysis reported elsewhere^{7,8}. The *Ca/P* ratio was obtained using the results of Rietveld refinement based on average multiplicity and occupancy values (*O*) of the *Ca1*, *Ca2* and *P* atoms in the unit cell of HAp according to equation 1.

$$\frac{Ca}{P} = \frac{(4 \times OCa1) + (6 \times OCa2)}{(6 \times OP)} \quad (1)$$

2.3.3. TEM

A HR-TEM study was carried out to evaluate the crystalline structure at the nanoscale level and complement the XRD structural analysis to identify the initial and final stages of apatite formation on BHAp and the BHAp/Nagel composite sintered ceramics. For TEM analysis, the ceramic samples were ground in an agate mortar to obtain fine powders and then immersed in Hank's solution for 0, 6 and 28 days. After exposure, the powders were dried in a muffle at 37 °C during 24 h. In all cases, the powder particles were dispersed in ethanol and deposited on a Cu holder. The prepared samples were measured in a transmission electron microscope (JEOL 2010F, Japan), equipped with a field emission electron gun and operated at 200 kV. Chemical analysis was carried out in a JEOL 2100 LaB6 Transmission Electron Microscope at 200 kV in STEM mode. Energy Dispersive Analysis of X-rays (EDX) was performed using an Oxford Instruments INCA X-sight with Si(Li) detector and the INCA Microanalysis suite (v.409).

2.3.4. Raman Spectroscopy

Raman spectra were recorded at room temperature before and after bioactivity tests in triplicate using a confocal Raman microscope (Bruker SENTERRA) with an excitation source of 532 nm. The measurements were carried out in the 300-3700 cm⁻¹ frequency range, at a spectral resolution of 0.5 cm⁻¹ and an integration time of 40 s.

3. Results and discussion

3.1. Morphological characterization (SEM)

The formation of an apatite layer on ceramic's surface was consistently monitored by SEM. Typical micrographs of BHAp and BHAp/Nagel composite before and after bioactivity tests are presented in figures 1 and 2.

Well-defined grain boundaries are observed in the as-sintered BHAp microstructure with a homogeneous grain size distribution of $1.58 \pm 0.21 \mu\text{m}$ and a surface porosity obtained by image analysis of $0.31 \pm 0.16 \%$ (figures 1a, e). In contrast, the as-sintered BHAp/Nagel composite sample showed porosities around $3.03 \pm 0.83 \%$. Two different kinds of microstructural features were identified, one coarse-grained microstructure with the presence of Si-rich precipitates with contents around 4.982 wt.% and Na-rich areas with contents around 6.450 wt.% (zone 1) was related to the formation of a secondary phase identified by XRD as Nagel, which was previously synthesized as a single phase with a composition of Na = 6.259 wt.% and Si = 4.899 wt.%. On the other hand, an homogeneous fine-grained microstructure (zone 2) corresponding to HAp was detected (See figure 2a, e), as reported in a previous work ⁸. In BHAp ceramics, after 6 days of exposure, dramatic changes in surface morphology were observed (figures 1b, f) as a result of an apatite layer formation. Two types of microstructures were detected at this exposure time, a layer with dune-like morphology and below this, a cracked surface with worm-like microstructure. The dune-like layer covered the entire ceramics surface after 14 days (figure 1c) showing a continuous growth of the spherical agglomerates, which after 28 days reached sizes around $4.5 \mu\text{m}$ (figure 1d). A closer look at the agglomerates after 14 and 28 days is shown in figures 1g and h, respectively. These agglomerates are formed by submicrometric plate-like crystals, which are growing as a function of immersion time, indicating the crystallization of the bone-like apatite layer ¹⁸.

For the BHAp/Nagel composite, a similar formation mechanism but with higher crystallization kinetic was observed in comparison with BHAp (see figure 2). Unlike the surface morphology of pure BHAp after 6 days, the correspondent of the BHAp/Nagel composite sample was already covered with a well-adhered apatite layer with spherical particles formed with small worm-like aggregates (figure 2b, f). After 14 and 28 days of immersion, the plate-like crystals, as well as the spherical agglomerates are more abundant than in BHAp samples.

1
2 The accelerated formation kinetics in BHAp/Nagel composite ceramics is mainly related to
3 the presence of Si in the BG, which promotes apatite precipitation due to the defects
4 formation in the HAp lattice (i.e., vacancies or substitutions) and therefore the generation of
5 a more electronegative surface⁴⁷, thus leading to an increase in surface solubility⁴⁸.
6
7

8
9 The EDX analysis showed an increase in Mg from 0.649 ± 0.049 wt. % to 1.407 ± 0.125 wt.
10 % and Na from 1.136 ± 0.138 wt. % to 2.945 ± 0.230 wt. %. In contrast, a decrease in Ca
11 content from 37.057 ± 0.962 wt. % to 28.781 ± 0.685 wt. % with layer growth on pure BHAp
12 samples was observed. No significant changes in P content were detected. Mg content
13 showed similar behavior in BHAp/Nagel composite samples, increasing from 0.268 ± 0.030
14 wt. % to 2.317 ± 1.202 wt. %, whereas Na decreases from 6.021 ± 0.403 wt. % to
15 3.028 ± 0.648 wt. % and a drop in P content from 22.245 ± 3.084 wt. % to 12.865 ± 0.986
16 wt. % was observed as the layer was grown. No significant variations in Ca content were
17 identified for the apatite grown on BHAp/Nagel composite samples.
18
19

20
21 The thickness of the apatite layer was evaluated in micrographs from ceramics cross-sections
22 after 14 (figures 3a, c) and 28 days (figures 3b, d) of exposure. A dense and well-adhered
23 layer was observed for both BHAp and BHAp/Nagel composite ceramics after 14 days.
24
25

26
27 The apatite final thickness is similar between BHAp (2.5 μm) and BHAp/Nagel composite
28 (2.7 μm) ceramics. However, for the BHAp/Nagel composite, after 28 immersion days the
29 layer clearly shows better adherence to the surface. The reason for that can be associated to
30 microstructures of Figure 3d compared to 3b from pure BHAp. In the BHAp/Nagel
31 composite sample the process of apatite formation occurred not only at the surface but also
32 inside the ceramic pores, possibly due to the presence of Nagel phase and the ionic presents
33 in BG. Thus, the pores act as binding sites to the growing apatite on BHAp/Nagel composite
34 samples. This effect can also be observed at the surface of the samples as a function of
35 soaking time (Figure 2). Similar mechanisms have been reported for bioactive silicate
36 ceramics with higher Si contents⁴.
37
38
39
40
41
42
43
44
45
46
47
48
49
50

51 **3.2. Structural characterization**

52 **3.2.1. GXRD**

53
54 The XRD measurements and Rietveld refinements were all consistently done from 10 to 70
55 2θ ($^\circ$). However, the XRD patterns for both samples were plotted in the range between 20-
56
57
58
59
60

52 (°) to spotlight the structural changes after Hank's solution immersion as shown in figure 4. The HAp ($\text{Ca}_{10}(\text{PO}_4)_6(\text{OH})_2$) was identified as the main phase in samples with BHAp (figure 4a) and 96.25%BHAp+3.75%BG (figure 4b), according to the JCPDS 9-432 card: $P6_3/m$ space group and lattice parameters $a = b = 9.432 \text{ \AA}$, $c = 6.881 \text{ \AA}$. Moreover, for the 3.75%BG sample, the Nagelschmidite ($\text{Ca}_{7-x}\text{Na}_x(\text{PO}_4)_{2+x}(\text{SiO}_4)_{2-x}$; $x \leq 2$) was identified as a secondary phase, based on the presence of two diffraction peaks at 31.36 and 33.66 °, that correspond to (026) and (220) planes, respectively ⁸.

For the Nagel phase, the crystallographic information was taken from ⁴⁹: $P6_1$ space group and lattice parameters $a = b = 10.6336(1) \text{ \AA}$, $c = 21.6422(3) \text{ \AA}$. As a result, a BHAp/BG mixture in a 0.968/0.032 weight ratio heat-treated at 1220 °C led to a partial phase transformation of BHAp to 32.74 wt. % of Nagel phase according to Eq. 1.



The Rietveld refinement allowed to calculate strains from a and c lattice parameters, crystallite size and Ca/P ratio before and after sample immersion for both compositions. These parameters varied due to the ionic exchange between the material surface and the medium, such as carbonates inclusion in the HAp lattice (Table 1) ^{50,51}.

A contraction of HAp lattice parameter a was observed in both cases, in comparison with the stoichiometric HAp due to substitutions in the atomic positions of Ca^{2+} for Na^+ , also reported by ⁵², that favors the carbonated apatite formation due to the Na^+ substitution, which destabilizes the charge of HAp structure, facilitating the substitution of PO_4^{3-} by CO_3^{2-} to balance the total charge ^{52,53} (see Table 1).

From these results, one can see that there are atomic substitutions that led to variations in lattice parameters before immersion, which are not only related to BG additions but also the HAp source (BHAp) ⁷. For BHAp and the BHAp/Nagel composite sample, the Ca/P ratios are lower than the stoichiometric value (1.67) showing Ca-deficient HAp in both cases, as expected for biological HAp ^{7,50}. These changes have a direct effect on the properties of HAp including an increase in solubility and biodegradability in physiological fluid ⁵⁴.

GXRD patterns of sintered ceramics exposed in Hank's solution showed an amorphization process described by a broadening of the main peaks that increases with immersion time. These peaks between 30.5 to 34.5 ° correspond to (002), (211), (030) planes and exhibited

1
2 specific variations (in-sets in figures 4a-b). For instance, the doublet observed in the (211)
3 plane decreases in intensity tending to form a single peak after 28 days.
4

5
6 On the other hand, the intensity of (002) plane increases as a function of immersion time,
7 which is characteristic of a texturization of the formed apatite associated with a crystal
8 growth along the *c*-axis from HAp structure. This behavior is related to the amorphization
9 and recrystallization processes that is the origin of apatite as a growing new crystalline phase.
10
11 The formed apatite has a similar structure to HAp but contains atomic substitutions such as
12
13 Mg^{2+} , Zn^{2+} , F^- , CO_3^{2-} , Cl^- or Na^+ ⁵⁵⁻⁵⁷.
14
15

16
17 The crystallite sizes decrease from 271.8 to 40.3 nm and from 347.7 to 41.7 nm for BHAp
18 and BHAp/Nagel composite ceramics, respectively. In both cases, crystallite sizes of the
19 formed apatites are very similar to that found in the mineral part of a mammalian bone, where
20 the *c*-axes of plate-shaped apatite crystals are well aligned with the long axes of the collagen
21 fibrils^{3,58,59}. On the other hand, after the immersion test the Ca/P ratio increase to 1.770 and
22 1.736 for BHAp and BHAp/Nagel composite samples, respectively. This behavior was
23 previously reported in^{60,61}, where the increase of carbonate content absorption led to an
24 increase of the apatite Ca/P ratio⁶¹.
25
26
27
28
29
30
31
32

33 3.2.2. TEM

34
35 Specific structural changes taking place in samples with compositions BHAp and
36 BHAp/Nagel composite during the immersion tests at 0, 6 and 28 days characterized by TEM
37 are described in this section.
38
39

40 *As-sintered*

41
42
43 Figures 5 and 6 show the HR-TEM micrographs with the IFFT and FFT analysis as well as
44 the SAED patterns of the samples before the immersion. Figures 5a and 6a reveal a highly
45 periodic arrangement of atoms; in both cases, lattice fringes correspond to a lattice spacing
46 of $d = 0.854$ nm as shown in insets figures 5aI and 6aI. The lattice fringes are close to the
47 theoretical value, $d_{(100)} = 0.8155$ nm according to JCPDS 9-432 card, where the slight
48 difference can be related to the ionic substitutions in BHAp from natural sources⁷. The SAED
49 pattern for BHAp was indexed considering the [001] zone axis of the HAp unit cell (figure
50 5b). This region is clearly arranged in a hexagonal shape and matches with the results from
51 the FFT images presented in the insets of figures 5a-II and 6a-II. The same hexagonal
52
53
54
55
56
57
58
59
60

1 structure was observed in several areas of the examined BHAp and BHAp/Nagel composite
2 samples. Additionally, the high crystallinity of BHAp and BHAp/Nagel composite samples
3 are in agreement with the narrow and intense peaks of the GXRD pattern (see Fig 4).
4
5

6 Debye rings were observed in the SAED pattern of a different region in BHAp/Nagel
7 composite sample (figure 6b) indicating the presence of a nanocrystalline phase. The analysis
8 of the interplanar distances resulted in the identification of Nagel phase with a lattice spacing
9 $d=0.247$ nm, which is comparable with the highest intensity peak of the theoretical (hkl) list
10 that corresponds to $d_{(220)}=0.265$ nm⁴⁹. This related, Rietveld refinement results for the
11 BHAp/Nagel composite sample showed a Nagel content around 32.74 wt.%, despite the low
12 intensity of the XRD peaks observed for this phase⁸.
13
14
15
16
17
18
19

20 *After 6 days of immersion*

21 After 6 days, a highly crystalline zone and a matrix in an amorphous state were distinguished
22 for both BHAp and BHAp/Nagel composite samples, presented in figures 7a and 8a,
23 respectively. From these micrographs, one can see that the crystalline BHAp substrate is
24 delimited by a dark zone from the newly formed apatite phase.
25
26
27
28
29

30 The corresponding FFT analysis of the crystalline zones from the BHAp and BHAp/Nagel
31 composite samples are shown in figures 7b-I and 8a-I, respectively. Amorphous zones were
32 determined by the absence of electron-diffraction patterns and are associated with an early
33 stage of the apatite formation. Crystalline zones correspond to the initial HAp phase of both
34 samples. For the BHAp/Nagel composite sample, apatite nanocrystals, which are randomly
35 embedded in the amorphous matrix were observed after 6 days (figure 8b). The apatite
36 nanocrystals lattice fringes were measured and labeled in the IFFT of figure 8c leading to a
37 $d=0.269$ nm spacing, which corresponds to the (030) plane based on the HAp structure, with
38 a theoretical value of $d = 0.271$ nm. In contrast, no crystals were observed within the
39 amorphous matrix in the BHAp sample after 6 days as shown in figure 7c.
40
41
42
43
44
45
46
47

48 *After 28 days of immersion*

49 After 28 days, elongated crystals with lengths between 20 and 100 nm were observed for
50 BHAp (figure 9a). These crystals (zone 1) grow from dark areas (zone 2) which have been
51 associated with the formation of ACP clusters^{37,38,62}. It has been reported that the geometry
52 of the growing crystals increase their length with CO₃²⁻ content⁶³. These growing crystals
53 are overlapped (see figure 9b) in which a single one has approx. 23 nm length and 10 nm
54
55
56
57
58
59
60

1
2 width. On the other hand, in Figure 9c the zone labeled as “*new amorphous apatite*” presented
3 absence of electron-diffraction patterns and the zone labeled as “*crystalline zone from mature*
4 *apatite*” presented a clear SAED of HAp structure (figure 9cI) with an interface between both
5 zones. The amorphous area was always located in the outer zone of the crystal. Crystalline
6 zones were observed along the crystals until the dark zone, which can be related to the apatite
7 recrystallization process and it’s inside out formation. Moreover, in figures 10a and 10b,
8 oriented apatite crystals embedded in an amorphous matrix were identified and measured,
9 which is consistent with the observations shown in the FFT (10a-II) and its corresponding
10 IFFT (10a-III). The measured lattice spacing of these crystals was around 0.34 nm, that
11 corresponds to the (002) plane of HAp with a theoretical value of 0.344 nm.
12
13

14
15 Moreover, formed apatite crystals showed different morphologies for BHAp/Nagel
16 composite sample. The morphology of these crystals shown in figures 11a and 11b has the
17 appearance of interconnected fibers joined by nanosized clusters, similar to ACP (indicated
18 by white arrows)^{37,38,62}, all grouped in a continuous and dense matrix with a well-defined
19 boundary. This fiber-like morphology has been previously observed for apatite formed on
20 Bioglass® and was described as needle-like micro-crystal weaving together flake-like
21 crystals^{26,28,64}. These areas are composed mostly of Si and Mg as identified by EDX. In our
22 case, the presence of Si is associated to SiO_4^{4-} due to BG additions, which affects the apatite
23 growth kinetics due to the formation of SiOH bonds and its polycondensation, favoring the
24 adsorption of $\text{Ca}+\text{PO}_4+\text{CO}_3$ ⁶⁵ and increasing the maturation rate of the crystals.
25
26

27
28 On the other hand, a significant density of parallel needle arrays was observed in figures 11c
29 and 11d, where the 1.56 Ca/P ratio evidenced the formation of calcium-deficient apatite,
30 typically identified in bioactive calcium phosphates⁶². At this stage, these needle-like crystals
31 have entirely merged with no space between the crystals, which are similar to those observed
32 in BHAp after 28 days. It is worth to mention that the composition and morphology of the
33 observed crystals by TEM are in agreement with the growth of plate-like crystals on dense
34 ceramics surfaces observed by SEM after 14 days of immersion (see inset in figure 2g).
35 Moreover, the compositional gradient detected in the EDX analysis of the cross-sectional
36 view also confirmed the TEM results showing a calcium-deficient apatite with higher Mg
37 contents.
38
39

40
41 Thus, all these features suggest a coupled mechanism of apatite formation between the Si-
42 containing and calcium phosphate phases.
43
44
45
46
47
48
49
50
51
52
53
54

1
2 Additionally, similar SAED patterns identified by FFT were exhibited in the newly formed
3 apatite zone (figure 12a-I) and the mature crystallized apatite zone (figure 12a-II). In both
4 cases, the SAED pattern confirmed at the surface the phase transformation of BHAp to
5 apatite. The lattice fringes associated to a $d = 0.238$ nm determined in figure 12a-I are similar
6 to those of figure 8c (early stages of apatite formation), confirming that the apatite
7 crystallization process starts with distances lower than 0.30 nm and finishes around 0.34 nm,
8 in which the crystals grow aligned with a preferred (002) orientation. This preferential
9 orientation can be related to the re-arrangement of HAp in the presence of Hank's solution,
10 generating a change in its orientation and promoting the preferential growth in new crystals.
11 The development of crystallinity is guided by the mature crystallized apatite surface as shown
12 by the alignment of the crystallographic c -axis along the nucleating surface, following the
13 preferred orientation in the (002) plane.
14
15
16
17
18
19
20
21
22

23 Finally, a closer look to the mature crystallized apatite zone is shown figure 12b, where a
24 higher density of crystals joined and immersed in the matrix is observed with lattice fringes
25 between $0.322 < d < 0.340$ nm. This effect of crystal coalescence has been described as the
26 formation of various calcified tissues and was referred as “crystal fusion”, in which the
27 junction and adhesion of two apatite crystals tend to form a single crystal ⁵¹, in our case
28 oriented in the c -axis direction. This effect has also been reported elsewhere, where the
29 crystals growth along the main axis of the collagen fibrils ³⁸.
30
31
32
33
34
35
36
37

38 3.2.3. Raman

39
40 Raman spectra of BHAp and BHAp/Nagel composite samples after 0, 6, 14 and 28 days of
41 exposure in Hank's solution are shown in figure 13a and b, respectively. Before exposure,
42 BHAp samples showed the typical vibrational modes associated with the phosphate
43 tetrahedral with $\nu_1 PO_4^{3-}$ band close to 962 cm^{-1} , a double $\nu_2 PO_4^{3-}$ band in 430 and 444 cm^{-1} ,
44 a triple $\nu_4 PO_4^{3-}$ band between 550 and 650 cm^{-1} , respectively. Specifically for $\nu_3 PO_4^{3-}$ only
45 three bands, typical for B-type carbonated apatite are observed in 1015 – 1090 cm^{-1} spectral
46 region ^{66,67}. Furthermore, the O-H stretching peak can be seen at 3572 cm^{-1} ¹².
47
48
49
50
51
52

53 Before immersion, BHAp/Nagel composite samples exhibited two types of spectra labeled
54 as 0 days “a” and “b” as shown in figure 13b. The spectrum “a” shows the same vibrational
55 modes than those observed for pure BHAp samples. On the other hand, in the spectrum “b”
56
57
58
59
60

1
2 a slight contribution Si-O vibrational mode was observed in 587, 615 and 853 cm^{-1} , which
3 are associated with the Nagel phase identified in XRD patterns ⁸.

4
5
6 After immersion in Hank's solution, similar behavior was observed for both BHAp and
7 BHAp/Nagel composite ceramics, but the changes were more evident in samples with BG
8 content. An increasing broadening and a continuous loss of intensity of the bands was
9 observed after 6, 14 and 28 days of immersion, which is related to the presence of non-
10 crystalline materials ⁴. Specifically, vibrations of $-\text{PO}_3$ and $-\text{PO}_2$ groups in amorphous
11 phosphate phases can be contributing to the broad-band between 1000 and 1300 cm^{-1} . On the
12 other hand, the presence of a broad-band around 1490 cm^{-1} can be related to carbonate ions
13 of amorphous carbonated hydroxyapatite phase as reported in ⁴. Moreover, in both samples
14 after 28 days of immersion, a wide band was detected in 1070 cm^{-1} , which has been assigned
15 to $\nu_1 \text{CO}_3^{2-}$ mode in B-Type carbonate HAp ⁶⁶.

16
17 For the BHAp/Nagel composite, the bands related to Si-O vibrational modes vanished after
18 6 days of immersion, this is expected since the mechanism of apatite formation in phases
19 containing Si involves the dissolution and precipitation of amorphous Si-phases ⁴.

20
21 These results evidenced the phase transformation from HAp and Nagel into a less crystalline
22 carbohydroxyapatite or bone-like apatite. Considering the bands' linewidths at the same
23 immersion periods for both evaluated sample compositions, it is evident that this
24 transformation occurred faster in the BHAp/Nagel composite. A summary of the vibrational
25 modes detected for both BHAp and BHAp/Nagel composite samples is presented in Table 2,
26 where the reported values for stoichiometric and carbonated B-Type HAp are also included
27 for comparative purposes.

28 29 30 31 32 33 34 35 36 37 38 39 40 41 42 43 44 **3.3. Degradation assessment**

45
46 The concentration of released ions after the degradation test is summarized and compared to
47 literature values in Table 3. The effect of BG addition resulted in close to double Ca and Na
48 dissolution in comparison with BHAp samples. Additionally, higher released Si content was
49 observed for the BHAp/Nagel composite as expected for the BG addition. The obtained
50 values for the analyzed species are within the range considered as no cytotoxic even in
51 combination with other ions ^{52,68}.

1
2 It is well known that dissolution of Si ions leads to the formation of a porous SiO₂ rich layer
3 on the surface of the powder, improving the readsorption of free ions of Ca, Mg and Si in
4 solution. As a consequence, a synergistic regulation is generated between the Ca, Si and Mg
5 ions during the dissolution process ⁶⁹. On the other hand, Ca ions tend to facilitate cell
6 proliferation, differentiation and mineralization of human periodontal ligament cells
7 (hPDL), osteoblasts and stem cells. Also, extracellular Ca plays a vital role in bone
8 remodeling by direct activation of intracellular mechanisms through the stimulation of Ca
9 detection receptors in osteoblastic cells ⁶⁸. Mg acts on the stimulation of cell proliferation by
10 promoting the synthesis of DNA, proteins and the regulation of Mg²⁺ conduction channels ²⁰.
11 The differences in ionic release of the samples suggest variations not only in the bioactive
12 behavior as discussed in the previous section but also in the biological response at the *in-*
13 *vitro* or *in-vivo* level.
14
15
16
17
18
19
20
21
22
23
24

25 **4. Conclusions**

26
27 The study of biomineralization process from bovine-derived HAp and BHAp/Nagel
28 composite allowed to complete/confirm the mechanism of apatite formation:
29

30
31 The formation of a hydrated amorphous matrix allows the ionic exchange between the
32 surrounding medium and the material surface. The incorporation of Ca²⁺ ions into the ceramic
33 surface leads to the formation of ACP clusters, which later develop into apatite nanocrystals.
34 These embedded nanocrystals are randomly oriented and later coalesce, aided by CO₃²⁻,
35 forming bigger crystals with a preferred orientation to *c*-axis, the same alignment observed
36 in natural apatite growth along collagen fibrils.
37
38
39
40

41 The apatite maturation process was monitored by HRTEM & IFFT leading to the following
42 remarks:
43
44

- 45 1) Crystals in the early stage of formation exhibited interplanar distances between 0.238
46 and 0.269 nm, while mature apatite crystals reach up to $d = 0.34$ nm, corresponding
47 to the (002) HAp plane.
48
- 49 2) The presence of Na⁺ in the degradation test favors the substitution of PO₄³⁻ for CO₃²⁻
50 promoting the release of Mg²⁺ and Ca²⁺. The new cation-rich surface attracts anions
51 from the fluid such as Cl⁻, F⁻, which in turn attracts cations and the cycle begins again,
52 thus generating a multi-layered growth.
53
54
55
56
57
58
59
60

- 1
2
3
4
5
6
7
8
9
10
11
12
13
14
15
16
17
18
19
20
- 3) BG addition allows the formation of nanocrystalline Nagel as a secondary phase in the 3.75 vol. %BG sample. The apatite formation results from a coupled mechanism between the Si-containing and calcium phosphate phases. The Nagel phase contributed to an accelerated formation kinetics observed with the apatite crystallization process and better adhesion of the apatite layer to the ceramic surface observed in the inward growth of apatite into the pores.
 - 4) After 28 days of exposure, the TEM images of the formed scale showed a highly periodic arrangement of the apatite crystals embedded in the amorphous matrix, which contrasts to the total amorphous characteristics reported for this layer at the macroscale.

21 Acknowledgments

22
23
24
25
26
27
28
29
30
31
32
33
34
35
36
37
38
39
40

The authors thank CONACYT for the financial support and the Spanish MINECO through project MAT2016-46755-R. This project was funded by CONACYT Projects 272095, 279738, 293429 and 295261 and carried out partially at CENAPROT (LN-299038) and LIDTRA (LN-295261 and LN-254119) national laboratories and LISMA. Additionally, we thank researchers Josep M^a Bassas and Lluís López Conesa of to the Scientific and Technological Centers of the University of Barcelona (CCiTUB) for technical support in the XRD and TEM measurements. Finally, the thanks are extended to David Andrés Fernandez-Benavides and Astrid Lorena Giraldo-Betancur for overall support.

41 References

- 42
43
44
45
46
47
48
49
50
51
52
53
54
55
56
57
58
59
60
- (1) Kokubo, T. Bioactive Glass Ceramics: Properties and Applications. *Biomaterials* **1991**, *12* (2), 155–163. [https://doi.org/10.1016/0142-9612\(91\)90194-F](https://doi.org/10.1016/0142-9612(91)90194-F).
 - (2) Ducheyne, P.; Qiu, Q. Bioactive Ceramics the Effect of Surface Reactivity on Bone Formation and Bone Cell Function. **1999**, *20*, 2287–2303.
 - (3) Müller, L.; Conforto, E.; Caillard, D.; Müller, F. A. Biomimetic Apatite Coatings-Carbonate Substitution and Preferred Growth Orientation. *Biomol. Eng.* **2007**, *24* (5), 462–466. <https://doi.org/10.1016/j.bioeng.2007.07.011>.
 - (4) Serena, S.; Caballero, A.; De Aza, P. N.; Sainz, M. A. New Evaluation of the in Vitro Response of Silicocarnotite Monophasic Material. *Ceram. Int.* **2015**, *41* (8), 9412–9419. <https://doi.org/10.1016/j.ceramint.2015.03.319>.

- 1
2 (5) Sepantafar, M.; Mohammadi, H.; Maheronnaghsh, R.; Tayebi, L.; Baharvand, H. Single Phased
3 Silicate-Containing Calcium Phosphate Bioceramics: Promising Biomaterials for Periodontal Repair.
4 *Ceram. Int.* **2018**. <https://doi.org/10.1016/j.ceramint.2018.03.050>.
5
6 (6) Wu, C.; Chang, J. A Review of Bioactive Silicate Ceramics. *Biomed. Mater.* **2013**, *8* (3).
7 <https://doi.org/10.1088/1748-6041/8/3/032001>.
8
9 (7) Rincón-López, J. A.; Hermann-Muñoz, J. A.; Giraldo-Betancur, A. L.; De Vizcaya-Ruiz, A.; Alvarado-
10 Orozco, J. M.; Muñoz-Saldaña, J. Synthesis, Characterization and in Vitro Study of Synthetic and
11 Bovine-Derived Hydroxyapatite Ceramics: A Comparison. *Materials (Basel)*. **2018**, *9* (3).
12 <https://doi.org/10.3390/ma11030333>.
13
14 (8) Rincón-López, J. A.; Hermann-Muñoz, J. A.; Fernández-Benavides, D. A.; Giraldo-Betancur, A. L.;
15 Alvarado-Orozco, J. M.; Muñoz-Saldaña, J. Isothermal Phase Transformations of Bovine-Derived
16 Hydroxyapatite/Bioactive Glass: A Study by Design of Experiments. *J. Eur. Ceram. Soc.* **2019**, *39* (4).
17 <https://doi.org/10.1016/j.jeurceramsoc.2018.11.021>.
18
19 (9) Jones, J. R. Review of Bioactive Glass : From Hench to Hybrids. *Acta Biomater.* **2013**, *9* (1), 4457–
20 4486. <https://doi.org/10.1016/j.actbio.2012.08.023>.
21
22 (10) Vallet-regí, M. *Bio-Ceramics with Clinical Applications*; Vallet-Regí, M., Ed.; Wiley, 2014.
23
24 (11) Serena, S.; Sainz, M. A.; Caballero, A. Single-Phase Silicocarnotite Synthesis in the Subsystem
25 $\text{Ca}_3(\text{PO}_4)_2\text{-Ca}_2\text{SiO}_4$. *Ceram. Int.* **2014**, *40* (6), 8245–8252.
26 <https://doi.org/10.1016/j.ceramint.2014.01.022>.
27
28 (12) Gomes, S.; Nedelec, J. M.; Jallot, E.; Sheptyakov, D.; Renaudin, G. Silicon Location in Silicate-
29 Substituted Calcium Phosphate Ceramics Determined by Neutron Diffraction. *Cryst. Growth Des.*
30 **2011**, *11* (9), 4017–4026. <https://doi.org/10.1021/cg200587s>.
31
32 (13) Landi, E.; Tampieri, A.; Mattioli-Belmonte, M.; Celotti, G.; Sandri, M.; Gigante, A.; Fava, P.; Biagini,
33 G. Biomimetic Mg- and Mg_3CO_3 -Substituted Hydroxyapatites: Synthesis Characterization and in Vitro
34 Behaviour. *J. Eur. Ceram. Soc.* **2006**, *26* (13), 2593–2601.
35 <https://doi.org/10.1016/j.jeurceramsoc.2005.06.040>.
36
37 (14) Furko, M.; Havasi, V.; Kónya, Z.; Grünewald, A.; Detsch, R.; Boccaccini, A. R.; Balázs, C.
38 Development and Characterization of Multi-Element Doped Hydroxyapatite Bioceramic Coatings on
39 Metallic Implants for Orthopedic Applications. *Boletín la Soc. Española Cerámica y Vidr.* **2017**.
40 <https://doi.org/https://doi.org/10.1016/j.bsecv.2017.09.003>.
41
42 (15) Fielding, G. A.; Bandyopadhyay, A.; Bose, S. Effects of Silica and Zinc Oxide Doping on Mechanical
43 and Biological Properties of 3D Printed Tricalcium Phosphate Tissue Engineering Scaffolds. *Dent.*
44 *Mater.* **2012**, *28* (2), 113–122. <https://doi.org/10.1016/j.dental.2011.09.010>.
45
46 (16) Boanini, E.; Torricelli, P.; Sima, F.; Axente, E.; Fini, M.; Mihailescu, I. N.; Bigi, A. Strontium and
47 Zoledronate Hydroxyapatites Graded Composite Coatings for Bone Prostheses. *J. Colloid Interface Sci.*
48 **2015**, *448*, 1–7. <https://doi.org/10.1016/j.jcis.2015.01.088>.
49
50
51
52
53
54
55
56
57
58
59
60

- 1
2 (17) Reffitt, D. M.; Jugdaohsingh, R.; Thompson, R. P. H.; Powell, J. J. Silicic Acid: Its Gastrointestinal
3 Uptake and Urinary Excretion in Man and Effects on Aluminium Excretion. *J. Inorg. Biochem.* **1999**,
4 *76* (2), 141–147. [https://doi.org/10.1016/S0162-0134\(99\)00126-9](https://doi.org/10.1016/S0162-0134(99)00126-9).
5
6 (18) Padilla, S.; Román, J.; Sánchez-salcedo, S.; M., V.-R. Hydroxyapatite / SiO₂ – CaO – P₂O₅ Glass
7 Materials: In Vitro Bioactivity and Biocompatibility. *Acta Biomater.* **2006**, No. June, 331–342.
8 <https://doi.org/10.1016/j.actbio.2006.01.006>.
9
10 (19) Gaharwar, A. K.; Mihaila, S. M.; Swami, A.; Patel, A.; Sant, S.; Reis, R. L.; Marques, A. P.; Gomes,
11 M. E.; Khademhosseini, A. Bioactive Silicate Nanoplatelets for Osteogenic Differentiation of Human
12 Mesenchymal Stem Cells. *Adv. Mater.* **2013**, *25* (24), 3329–3336.
13 <https://doi.org/10.1002/adma.201300584>.
14
15 (20) Zreiqat, H.; Howlett, C. R.; Zannettino, A.; Evans, P.; Schulze-Tanzil, G.; Knabe, C.; Shakibaei, M.
16 Mechanisms of Magnesium-Stimulated Adhesion of Osteoblastic Cells to Commonly Used
17 Orthopaedic Implants. *J. Biomed. Mater. Res.* **2002**, *62* (2), 175–184.
18 <https://doi.org/10.1002/jbm.10270>.
19
20 (21) Barakat, N. A. M.; Khil, M. S.; Omran, A. M.; Sheikh, F. A.; Kim, H. Y. Extraction of Pure Natural
21 Hydroxyapatite from the Bovine Bones Bio Waste by Three Different Methods. *J. Mater. Process.*
22 *Technol.* **2009**, *209* (7), 3408–3415. <https://doi.org/10.1016/j.jmatprotec.2008.07.040>.
23
24 (22) Piña, C.; Palma, B.; Munguía, N.; Piña, C.; Palma, B.; Munguía, N. Material Properties of Inorganic
25 Bovine Cancellous Bovine : Nukbone. **2006**, *221*, 1–4. <https://doi.org/10.1063/1.2356454>.
26
27 (23) Kattimani, V. S.; Kondaka, S.; Lingamaneni, K. P. Hydroxyapatite—Past, Present, and Future in Bone
28 Regeneration. *Bone Tissue Regen. Insights* **2016**, *7*, BTRIS36138.
29 <https://doi.org/10.4137/BTRIS36138>.
30
31 (24) Maçon, A. L. B.; Kim, T. B.; Valliant, E. M.; Goetschius, K.; Brow, R. K.; Day, D. E.; Hoppe, A.;
32 Boccaccini, A. R.; Kim, I. Y.; Ohtsuki, C.; et al. A Unified in Vitro Evaluation for Apatite-Forming
33 Ability of Bioactive Glasses and Their Variants. *J. Mater. Sci. Mater. Med.* **2015**, *26* (2), 1–10.
34 <https://doi.org/10.1007/s10856-015-5403-9>.
35
36 (25) Kim, H. M.; Himeno, T.; Kokubo, T.; Nakamura, T. Process and Kinetics of Bonelike Apatite
37 Formation on Sintered Hydroxyapatite in a Simulated Body Fluid. *Biomaterials* **2005**, *26* (21), 4366–
38 4373. <https://doi.org/10.1016/j.biomaterials.2004.11.022>.
39
40 (26) Kumar, A.; Murugavel, S.; Aditya, A.; Boccaccini, A. R. Mesoporous 45S5 Bioactive Glass: Synthesis,
41 In Vitro Dissolution and Biomineralization Behavior. *J. Mater. Chem. B* **2017**, *5* (44), 8786–8798.
42 <https://doi.org/10.1039/c7tb01738c>.
43
44 (27) Gandolfi, M. G.; Ciapetti, G.; Taddei, P.; Perut, F.; Tinti, A.; Cardoso, M. V.; Van Meerbeek, B.; Prati,
45 C. Apatite Formation on Bioactive Calcium-Silicate Cements for Dentistry Affects Surface Topography
46 and Human Marrow Stromal Cells Proliferation. *Dent. Mater.* **2010**, *26* (10), 974–992.
47 <https://doi.org/10.1016/j.dental.2010.06.002>.
48
49
50
51
52
53
54
55
56
57
58
59
60

- 1
2 (28) Boccaccini, A. R.; Chen, Q.; Lefebvre, L.; Gremillard, L.; Chevalier, J. Sintering, Crystallisation and
3 Biodegradation Behaviour of Bioglass®-Derived Glass-Ceramics. *Faraday Discuss.* **2007**, *136*, 27–44.
4 <https://doi.org/10.1039/b616539g>.
5
6 (29) Zadpoor, A. A. Relationship between in Vitro Apatite-Forming Ability Measured Using Simulated
7 Body Fluid and in Vivo Bioactivity of Biomaterials. *Mater. Sci. Eng. C* **2014**, *35*, 134–143.
8 <https://doi.org/10.1016/j.msec.2013.10.026>.
9
10 (30) Æ, T. K.; Takadama, H. How Useful Is SBF in Predicting in Vivo Bone Bioactivity? *J. Biomed. Mater. Res. Part B: Appl. Biomater.* **2006**, *77*, 2907–
11 2915. <https://doi.org/10.1016/j.jbmb.2006.01.017>.
12
13 (31) Kim, H.-M.; Himeno, T.; Kawashita, M.; Kokubo, T.; Nakamura, T. The Mechanism of
14 Biomaterialization of Bone-like Apatite on Synthetic Hydroxyapatite: An in Vitro Assessment. *J. R. Soc. Interface* **2004**, *1* (1), 17–22. <https://doi.org/10.1098/rsif.2004.0003>.
15
16 (32) Hench, L. L. Bioactive Materials. *Ceram. Int.* **1996**, *22* (5), 493–507.
17
18 (33) Takadama, H.; Kim, H. M.; Kokubo, T.; Nakamura, T. Mechanism of Biomaterialization of Apatite on
19 a Sodium Silicate Glass: TEM-EDX Study in Vitro. *Chem. Mater.* **2001**, *13* (3), 1108–1113.
20 <https://doi.org/10.1021/cm0008718>.
21
22 (34) Vallet-Regí, María; Izquierdo-Barba, I. S. A. J. Influence of P₂O₅ on Crystallinity of Apatite Formed
23 in Vitro on Surface of Bioactive Glasses. **1999**.
24
25 (35) Leng, Y.; Chen, J.; Qu, S. TEM Study of Calcium Phosphate Precipitation on HA/TCP Ceramics.
26 *Biomaterials* **2003**, *24* (13), 2125–2131. [https://doi.org/10.1016/S0142-9612\(03\)00036-X](https://doi.org/10.1016/S0142-9612(03)00036-X).
27
28 (36) Takadama, H.; Kim, H. M.; Miyaji, F.; Kokubo, T.; Nakamura, T. Mechanism of Apatite Formation
29 Induced by Silanol Groups - TEM Observation. *J. Ceram. Soc. Japan* **2000**, *108* (2), 118–121.
30 https://doi.org/10.2109/jcersj.108.1254_118.
31
32 (37) He, G.; Dahl, T.; Veis, A.; George, A. Nucleation of Apatite Crystals in Vitro by Self-Assembled Dentin
33 Matrix Protein 1. *Nat. Mater.* **2003**, *2* (8), 552–558. <https://doi.org/10.1038/nmat945>.
34
35 (38) Dey, A.; Bomans, P. H. H.; Müller, F. A.; Will, J.; Frederik, P. M.; De With, G.; Sommerdijk, N. A. J.
36 M. The Role of Prenucleation Clusters in Surface-Induced Calcium Phosphate Crystallization. *Nat. Mater.* **2010**, *9* (12), 1010–1014. <https://doi.org/10.1038/nmat2900>.
37
38 (39) Wang, Y.; Azaïs, T.; Robin, M.; Vallée, A.; Catania, C.; Legriel, P.; Pehau-Arnaudet, G.; Babonneau,
39 F.; Giraud-Guille, M. M.; Nassif, N. The Predominant Role of Collagen in the Nucleation, Growth,
40 Structure and Orientation of Bone Apatite. *Nat. Mater.* **2012**, *11* (8), 724–733.
41 <https://doi.org/10.1038/nmat3362>.
42
43 (40) Aizawa, M.; Porter, A. E.; Best, S. M.; Bonfield, W. Ultrastructural Observation of Single-Crystal
44 Apatite Fibres. *Biomaterials* **2005**, *26* (17), 3427–3433.
45 <https://doi.org/10.1016/j.biomaterials.2004.09.044>.
46
47 (41) Zhuang, Z.; Miki, T.; Yumoto, M.; Konishi, T.; Aizawa, M. Ultrastructural Observation of
48
49
50
51
52
53
54
55
56
57
58
59
60

- 1
2 Hydroxyapatite Ceramics with Preferred Orientation to A-Plane Using High-Resolution Transmission
3 Electron Microscopy. *Procedia Eng.* **2012**, *36*, 121–127. <https://doi.org/10.1016/j.proeng.2012.03.019>.
- 4
5 (42) Xin, R.; Leng, Y.; Wang, N. In Situ TEM Examinations of Octacalcium Phosphate to Hydroxyapatite
6 Transformation. *J. Cryst. Growth* **2006**, *289* (1), 339–344.
7 <https://doi.org/10.1016/j.jcrysgro.2005.11.010>.
- 8
9
10 (43) Xin, R.; Zhang, Q.; Gao, J. Identification of the Wollastonite Phase in Sintered 45S5 Bioglass and Its
11 Effect on in Vitro Bioactivity. *J. Non. Cryst. Solids* **2010**, *356* (23–24), 1180–1184.
12 <https://doi.org/10.1016/j.jnoncrysol.2010.03.010>.
- 13
14
15 (44) AG., S. <https://www.schott.com/epackaging/english/bioactive/products/cosmetics.html>.
- 16
17 (45) ISO. *ISO/FDIS 23317: Implants for Surgery-In Vitro Evaluation for Apatite-Forming Ability of Implant*
18 *Materials*; 2007; p 42. <https://doi.org/ISO/FDIS 22000>.
- 19
20 (46) Iso. *ISO 10993: Biological Evaluation of Medical Devices — Part 14: Identification and Quantification*
21 *of Degradation Products from Ceramics*; 2002.
- 22
23 (47) Vandiver, J.; Dean, D.; Patel, N.; Botelho, C.; Best, S.; Santos, J. D.; Lopes, M. A.; Bonfield, W.; Ortiz,
24 C. Silicon Addition to Hydroxyapatite Increases Nanoscale Electrostatic, van Der Waals, and Adhesive
25 Interactions. *J. Biomed. Mater. Res. Part A* **2006**. <https://doi.org/10.1002/jbm.a>.
- 26
27
28 (48) Yu, H.; Liu, K.; Zhang, F.; Wei, W.; Chen, C.; Huang, Q. Microstructure and in Vitro Bioactivity of
29 Silicon-Substituted Hydroxyapatite. *Silicon* **2017**, *9* (4), 543–553. [https://doi.org/10.1007/s12633-015-](https://doi.org/10.1007/s12633-015-9298-3)
30 [9298-3](https://doi.org/10.1007/s12633-015-9298-3).
- 31
32
33 (49) Widmer, R.; Gfeller, F.; Armbruster, T. Structural and Crystal Chemical Investigation of Intermediate
34 Phases in the System Ca₂SiO₄-Ca₃(PO₄)₂-CaNaPO₄. *J. Am. Ceram. Soc.* **2015**, *98* (12), 3956–3965.
35 <https://doi.org/10.1111/jace.13850>.
- 36
37
38 (50) T, B. W.; Pasteris, J. D. A Mineralogical Perspective on the Apatite in Bone. **2005**, *25*, 131–143.
39 <https://doi.org/10.1016/j.msec.2005.01.008>.
- 40
41 (51) Rey, C.; Combes, C.; Drouet, C.; Sfihi, H.; Barroug, A. Physico-Chemical Properties of Nanocrystalline
42 Apatites: Implications for Biominerals and Biomaterials. *Mater. Sci. Eng. C* **2007**, *27* (2), 198–205.
43 <https://doi.org/10.1016/j.msec.2006.05.015>.
- 44
45
46 (52) Sang Cho, J.; Um, S. H.; Su Yoo, D.; Chung, Y. C.; Hye Chung, S.; Lee, J. C.; Rhee, S. H. Enhanced
47 Osteoconductivity of Sodium-Substituted Hydroxyapatite by System Instability. *J. Biomed. Mater. Res.*
48 *- Part B Appl. Biomater.* **2014**, *102* (5), 1046–1062. <https://doi.org/10.1002/jbm.b.33087>.
- 49
50
51 (53) Peroos, S.; Du, Z.; De Leeuw, N. H. A Computer Modelling Study of the Uptake, Structure and
52 Distribution of Carbonate Defects in Hydroxy-Apatite. *Biomaterials* **2006**, *27* (9), 2150–2161.
53 <https://doi.org/10.1016/j.biomaterials.2005.09.025>.
- 54
55
56 (54) Lala, S.; Ghosh, M.; Das, P. K.; Das, D.; Kar, T.; Pradhan, S. K. Magnesium Substitution in Carbonated
57 Hydroxyapatite: Structural and Microstructural Characterization by Rietveld's Refinement. *Mater.*
58
59
60

- 1
2 *Chem. Phys.* **2016**, *170*, 319–329. <https://doi.org/10.1016/j.matchemphys.2015.12.058>.
- 3
- 4 (55) Elliott, J. C.; Wilson, R. M.; Dowker, S. E. P. APATITE STRUCTURES. **2002**, *45* (c), 172–181.
- 5
- 6 (56) Liu, Q.; Huang, S.; Matinlinna, J. P.; Chen, Z.; Pan, H. Review Article Insight into Biological Apatite :
7 Physiochemical Properties and Preparation Approaches. **2013**, *2013*.
- 8
- 9 (57) Akram, M.; Ahmed, R.; Shakir, I.; Ibrahim, W. A. W.; Hussain, R. Extracting Hydroxyapatite and Its
10 Precursors from Natural Resources. *J. Mater. Sci.* **2014**, *49* (4), 1461–1475.
11 <https://doi.org/10.1007/s10853-013-7864-x>.
- 12
- 13 (58) Müller, F. A.; Müller, L.; Caillard, D.; Conforto, E. Preferred Growth Orientation of Biomimetic
14 Apatite Crystals. *J. Cryst. Growth* **2007**, *304* (2), 464–471.
15 <https://doi.org/10.1016/j.jcrysgro.2007.03.014>.
- 16
- 17 (59) Nakano, T.; Kaibara, K.; Tabata, Y.; Nagata, N.; Enemoto, S.; Marukawa, E.; Umakoshi, Y. Unique
18 Alignment and Texture of Biological Apatite Crystallites in Typical Calcified Tissues Analyzed by
19 Microbeam X-Ray Diffractometer System. *Bone* **2002**, *31* (4), 479–487.
- 20
- 21 (60) Aizawa, M.; Matsuura, T.; Zhuang, Z. Syntheses of Single-Crystal Apatite Particles with Preferred
22 Orientation to the a- and c-Axes as Models of Hard Tissue and Their Applications. *Biol. Pharm. Bull.*
23 **2013**, *36* (11), 1654–1661. <https://doi.org/10.1248/bpb.b13-00439>.
- 24
- 25 (61) Aizawa, M.; Ueno, H.; Itatani, K.; Okada, I. Syntheses of Calcium-Deficient Apatite Fibres by a
26 Homogeneous Precipitation Method and Their Characterizations. *J. Eur. Ceram. Soc.* **2006**, *26* (4–5),
27 501–507. <https://doi.org/10.1016/j.jeurceramsoc.2005.07.007>.
- 28
- 29 (62) Eanes, E. D.; Termine, J. D.; Nysten, M. U. An Electron Microscopic Study of the Formation of
30 Amorphous Calcium Phosphate and Its Transformation to Crystalline Apatite. *Calcif. Tissue Res.* **1973**,
31 *12* (1), 143–158. <https://doi.org/10.1007/BF02013730>.
- 32
- 33 (63) Liao, S.; Watari, F.; Xu, G.; Ngiam, M.; Ramakrishna, S.; Chan, C. K. Morphological Effects of Variant
34 Carbonates in Biomimetic Hydroxyapatite. *Mater. Lett.* **2007**, *61* (17), 3624–3628.
35 <https://doi.org/10.1016/j.matlet.2006.12.007>.
- 36
- 37 (64) Zhong, J. P.; Greenspan, D. C.; Feng, J. W. A Microstructural Examination of Apatite Induced by
38 Bioglass® in Vitro. *J. Mater. Sci. Mater. Med.* **2002**, *13* (3), 321–326.
39 <https://doi.org/10.1023/A:1014075320987>.
- 40
- 41 (65) Hench, L. L. Bioceramics. *Stress Int. J. Biol. Stress* **1998**, *28*, 1705–1728.
42 <https://doi.org/10.1111/j.1151-2916.1998.tb02540.x>.
- 43
- 44 (66) Penel, G.; Leroy, G.; Rey, C.; Bres, E. MicroRaman Spectral Study of the PO₄ and CO₃ Vibrational
45 Modes in Synthetic and Biological Apatites. *Calcif. Tissue Int.* **1998**, *63* (6), 475–481.
46 <https://doi.org/10.1007/s002239900561>.
- 47
- 48 (67) Antonakos, A.; Liarokapis, E.; Leventouri, T. Micro-Raman and FTIR Studies of Synthetic and Natural
49 Apatites. *Biomaterials* **2007**, *28* (19), 3043–3054. <https://doi.org/10.1016/j.biomaterials.2007.02.028>.
- 50
- 51
- 52
- 53
- 54
- 55
- 56
- 57
- 58
- 59
- 60

- 1
2 (68) Zhang, M.; Chen, X.; Pu, X.; Liao, X.; Huang, Z.; Yin, G. Dissolution Behavior of
3 CaO-MgO-SiO₂-based Multiphase Bioceramic Powders and Effects of the Released Ions on
4 Osteogenesis. *J. Biomed. Mater. Res. Part A* **2017**, No. 24, 1–36.
5
6 (69) Saravanapavan, P.; Jones, J. R.; Pryce, R. S.; Hench, L. L. Bioactivity of Gel – Glass Powders in the
7 CaO-SiO₂ System : A Comparison with Ternary (CaO-P₂O₅-SiO₂) and Quaternary Glasses (SiO₂
8 -CaO-P₂O₅-Na₂O). **2002**, 17–19.
9
10
11
12
13
14
15
16
17
18
19
20
21
22
23
24
25
26
27
28
29
30
31
32
33
34
35
36
37
38
39
40
41
42
43
44
45
46
47
48
49
50
51
52
53
54
55
56
57
58
59
60

Figure Caption

- Figure 1.** Morphological changes on BHAp ceramics surface before (a,e) and after 6 (b,f), 14 (c,g) and 28 (d,h) days of exposure to Hank's solution.
- Figure 2.** Morphological changes on BHAp/Nagel composite ceramics surface before (a,e) and after 6 (b,f), 14 (c,g) and 28 (d,h) days of exposure to Hank's solution.
- Figure 3.** Cross-section micrographs showing the apatite layer thickness and composition after 14 and 28 days of immersion in Hank's solution of (a,b) BHAp and (c,d) BHAp/Nagel composite ceramics. The arrows indicate the apatite growing into the pores.
- Figure 4.** XRD pattern plotted between 20 – 52 2θ ($^{\circ}$) of a) BHAp and b) BHAp/Nagel composite ceramics after 0, 6, 14 and 28 days of immersion.
- Figure 5a.** High resolution TEM images, Inverse FFT (I) and FFT (II) of BHAp before bioactivity test.
- Figure 5b.** SAED pattern of BHAp before bioactivity test.
- Figure 6a.** High resolution TEM, Inverse FFT (I) and FFT (II) images of BHAp/Nagel composite before bioactivity test.
- Figure 6b.** SAED pattern of a nanocrystalline region of BHAp/Nagel composite before bioactivity test.
- Figure 7.** High resolution TEM images of BHAp after 6 days of exposure in Hank's solution, showing in a) morphology of the particles composed by b) crystalline zones (inset FFT image) and c) an amorphous matrix.
- Figure 8.** High resolution TEM images showing a) BHAp/Nagel composite particles after 6 days of immersion and b) closer look to the amorphous matrix. I and II show FFT images and profile of the marked zones.
- Figure 9.** High resolution TEM of a) BHAp particles after 28 days of exposure, b) zoom on the elongated crystals c) closer look to the interface between amorphous matrix and crystalline zone (inset FFT).
- Figure 10.** a,b) High resolution TEM images of different areas of BHAp particles after 28 days of immersion with apatite nanocrystals embedded. II and III show FFT images and IFFT of the marked zone I.
- Figure 11.** High resolution TEM of different areas of BHAp/Nagel composite particles after 28 days of exposure.
- Figure 12.** a,b) High resolution TEM images of different areas of BHAp/Nagel composite particles after 28 days of immersion. I-II show FFT images of the marked zones, and III corresponds to IFFT of region I.
- Figure 13.** Raman spectra of a) BHAp and b) BHAp/Nagel composite after different periods of immersion in Hank's solution.

Table caption

Table 1. Lattice parameters, crystallite size, cell volume, Ca/P ratio, goodness coefficient (χ^2) and structure factor (R_f) obtained from Rietveld refinement, for BHAp and BHAp/Nagel composite samples before and after immersion

Table 2. Comparison of Raman band assignments reported for stoichiometric HAp, carbonated HAp Type B, and experimental values from BHAp and BHAp/Nagel composite after 0, 6, 14 and 28 days of immersion in Hank's solution

Table 3. Ionic concentrations in the soaking solution before and after the degradation test. The concentrations considered cytotoxic are included for comparative purposes.

For Table of Contents Use Only

Preferred growth orientation of apatite crystals on biological hydroxyapatite enriched with bioactive glass: a biomimetic behavior

July Andrea Rincón-López ¹, Jennifer Andrea Hermann-Muñoz ¹, Núria Cinca-Luis ²,
Beatriz Garrido-Domiguez ², Irene García-Cano ², Jose Maria Guilemany-Casadamon ²,
Juan Manuel Alvarado-Orozco ^{3,4*}, Juan Muñoz-Saldaña ^{1*}

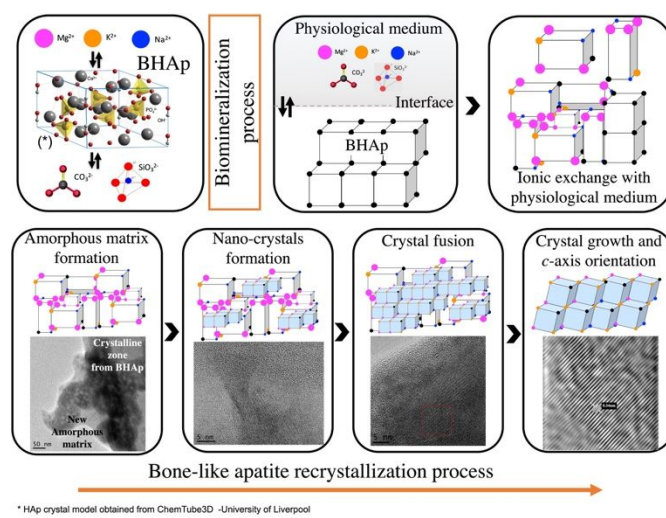
¹ Centro de Investigación y de Estudios Avanzados del IPN, Unidad Querétaro, Libramiento Norponiente #2000, Querétaro, Qro., C.P. 76230, México.

² Centro de Proyección Térmica (CPT). Dpt. Ciència dels Materials i Química Física, Universitat de Barcelona, c/Martí i Franquès 1, E-08028 Barcelona, Spain.

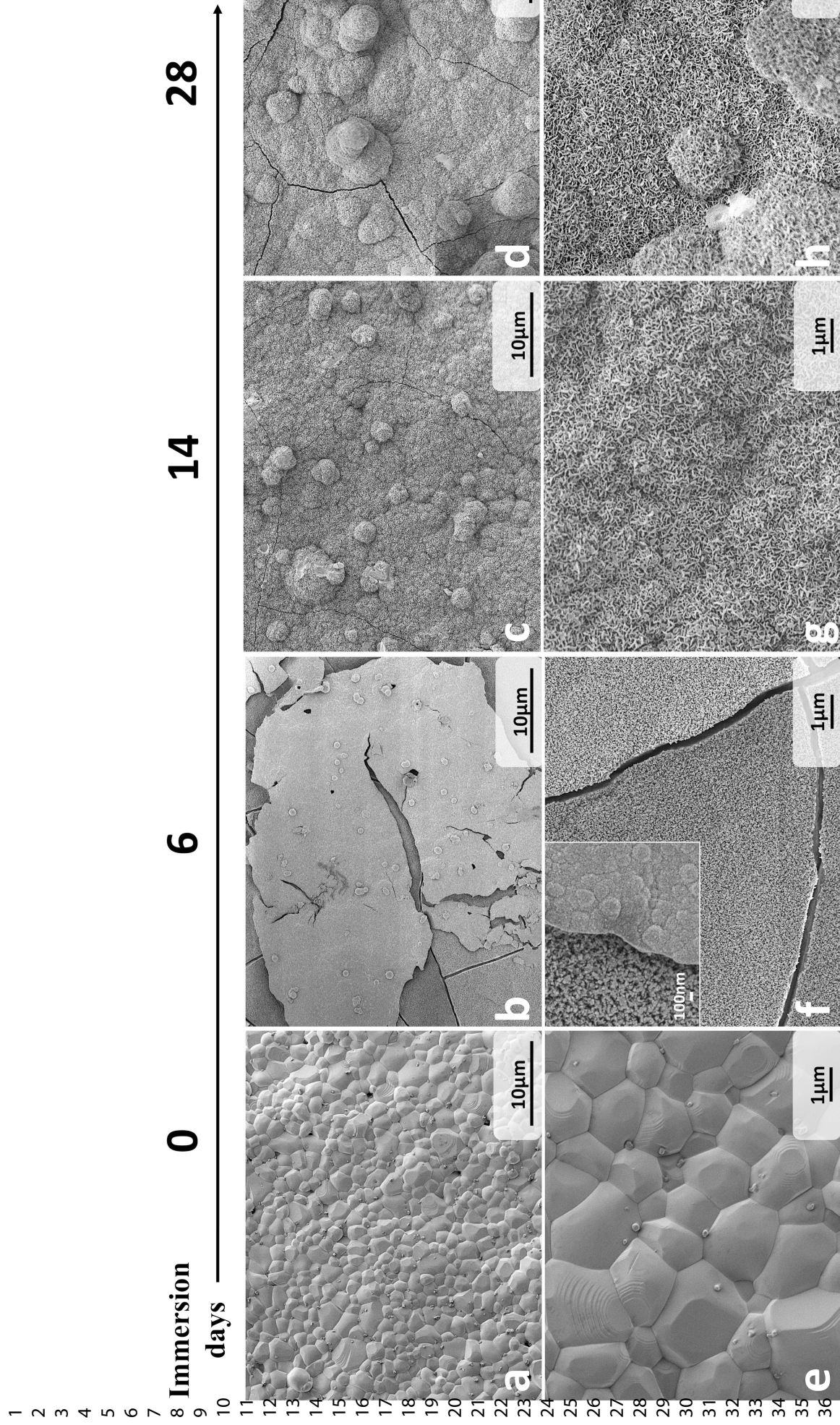
³ Centro de Ingeniería y Desarrollo Industrial, Av. Playa Pie de la Cuesta No. 702, Desarrollo San Pablo, Querétaro, Qro., C.P. 76125, México.

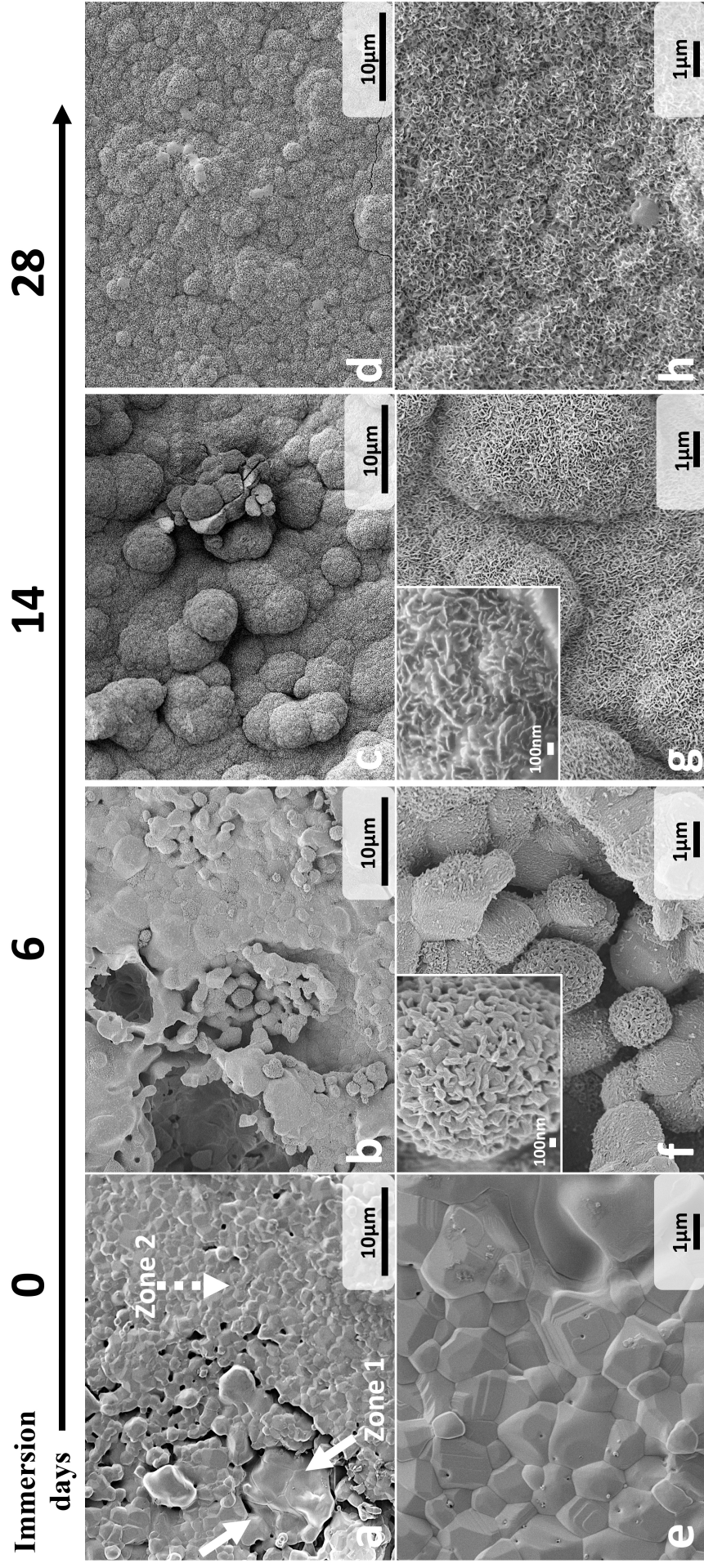
⁴ Consorcio de Manufactura Aditiva, CONMAD, Av. Pie de la Cuesta 702, Desarrollo San Pablo, Querétaro, México.

* Corresponding authors: juan.alvarado@cidesi.edu.mx, jmunoz@cinvestav.mx

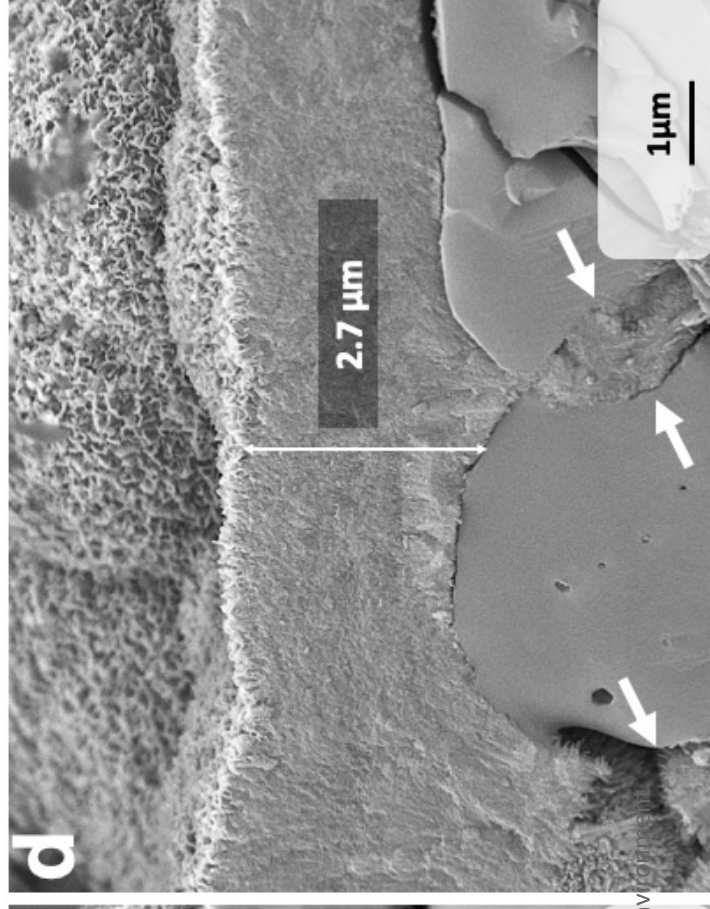
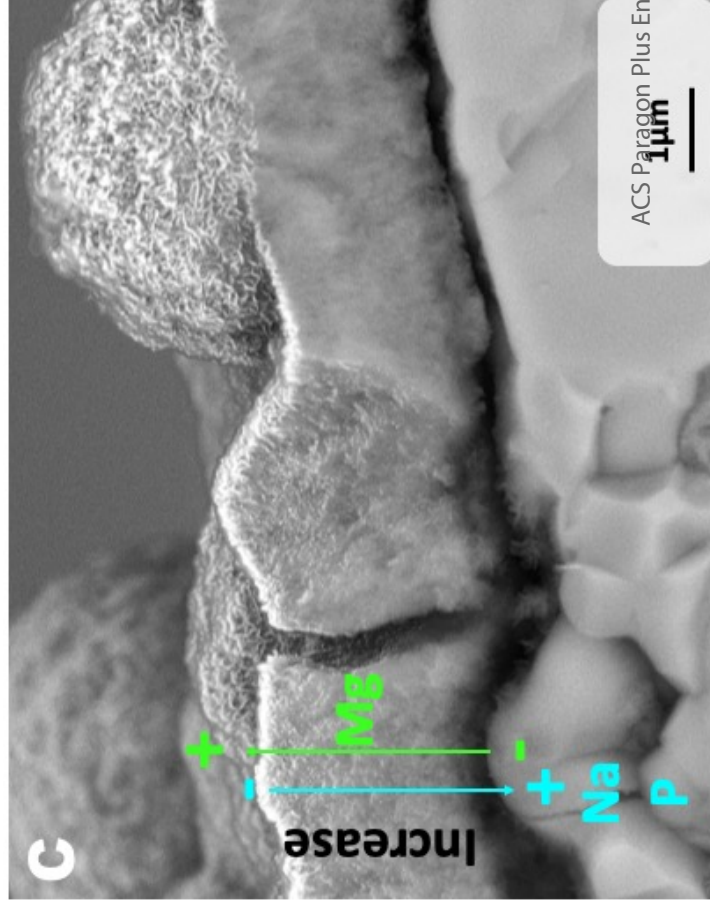
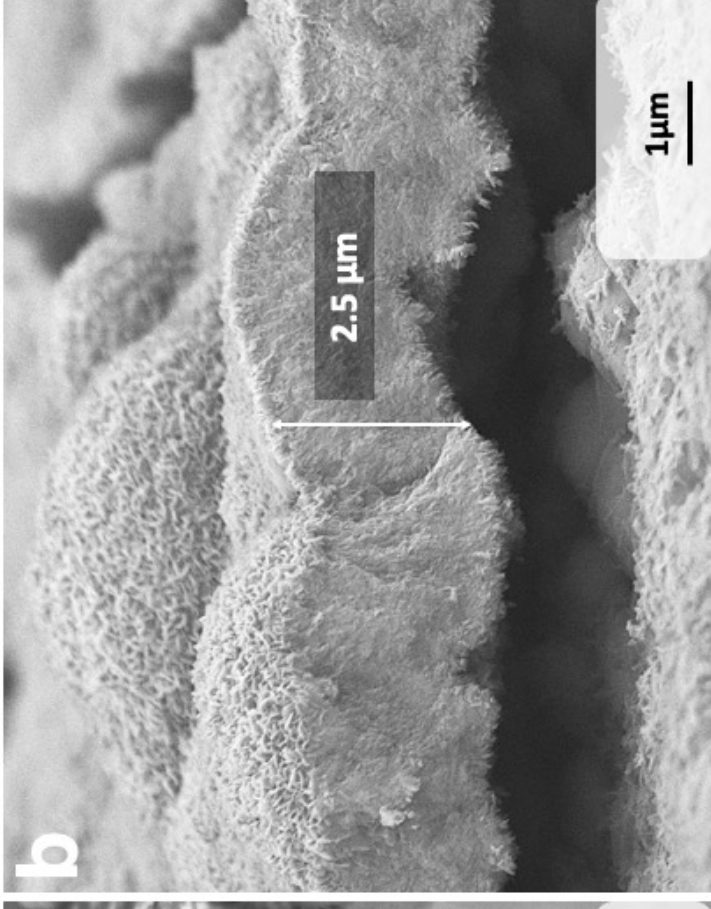
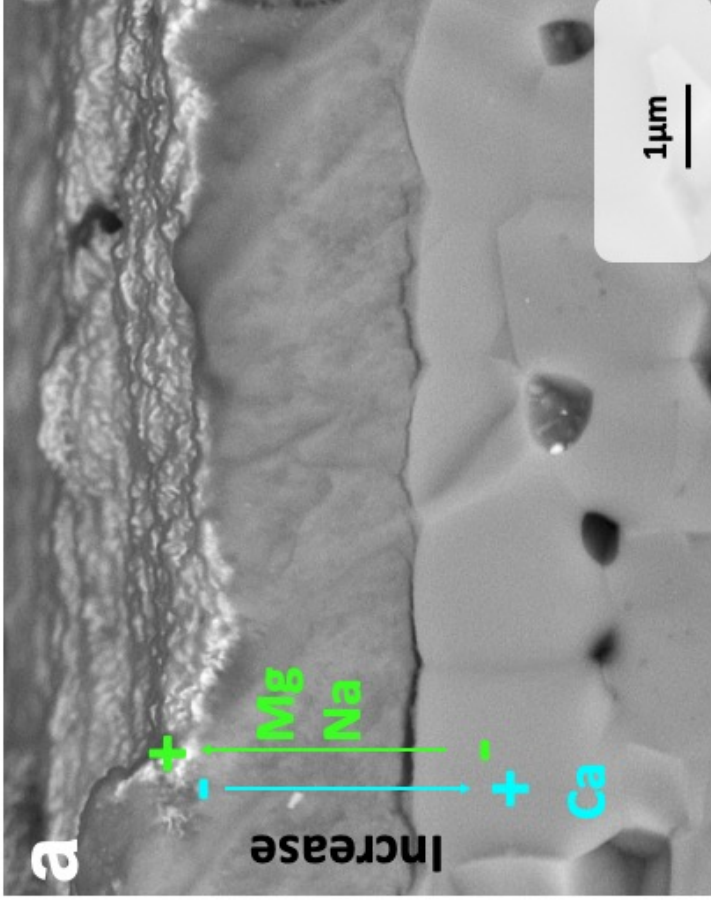


This contribution presents morphological, structural and chemical transformations during the biomaterialization process of BHAp enriched with Vitryxx® bioactive glass, where the mechanism of mineral matrix formation at the nano- and micro-scale is discussed. A highly periodic arrangement of the apatite crystals at the local level was observed with an accelerated apatite crystallization process due to the presence of Nagel phase.

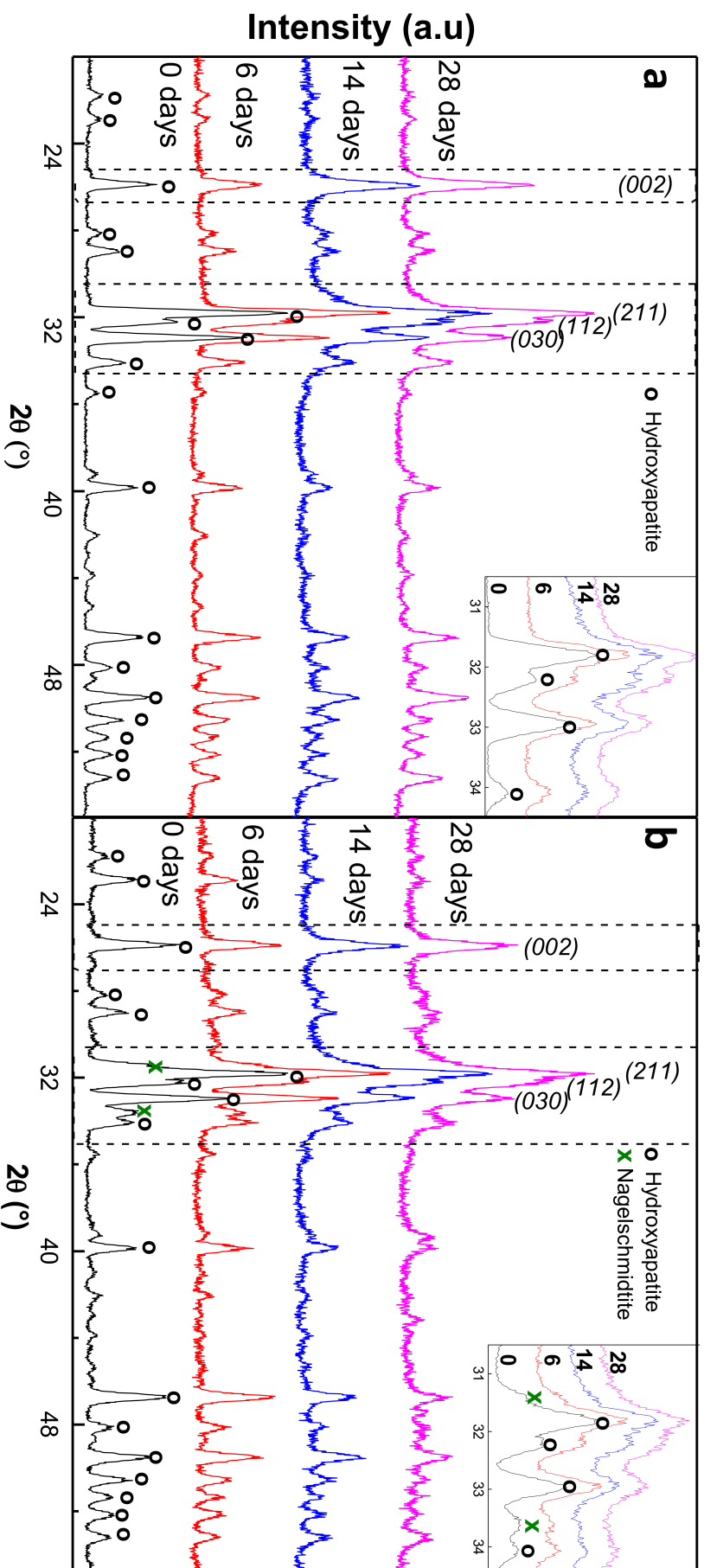


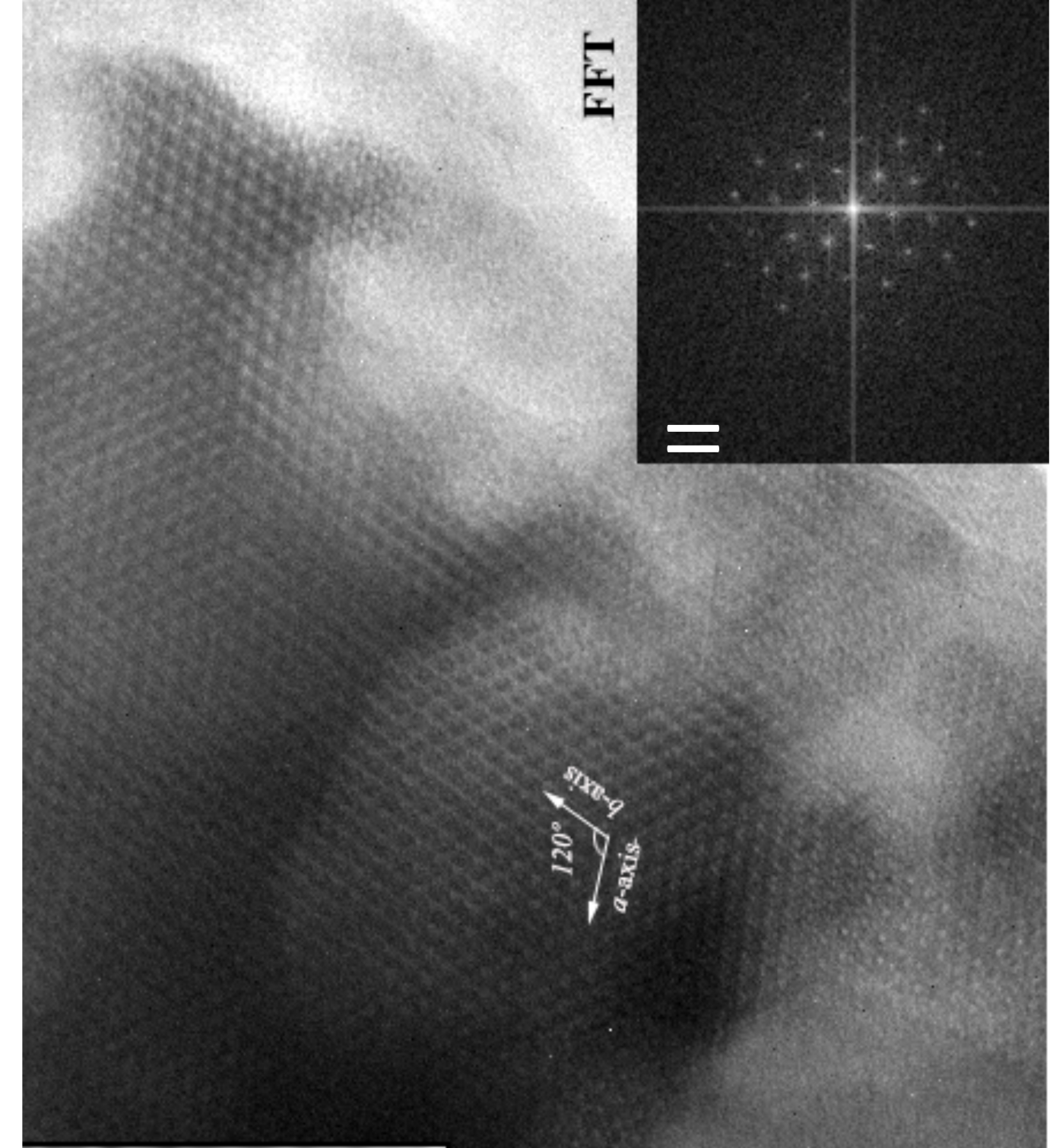
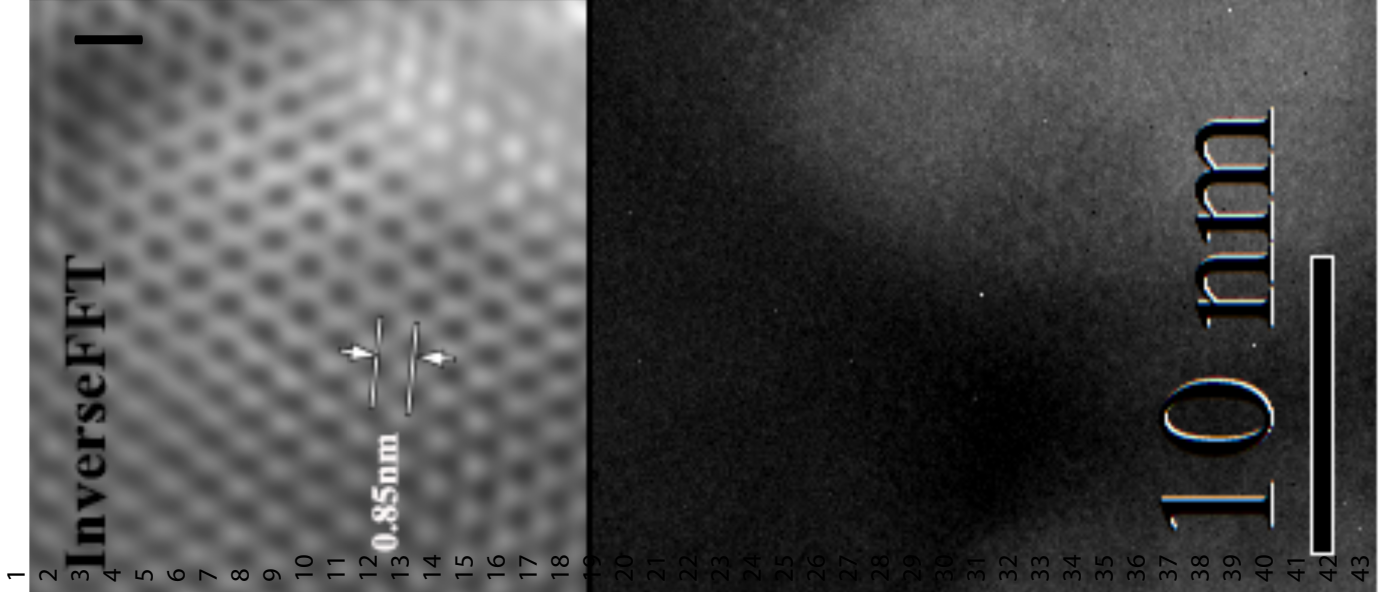


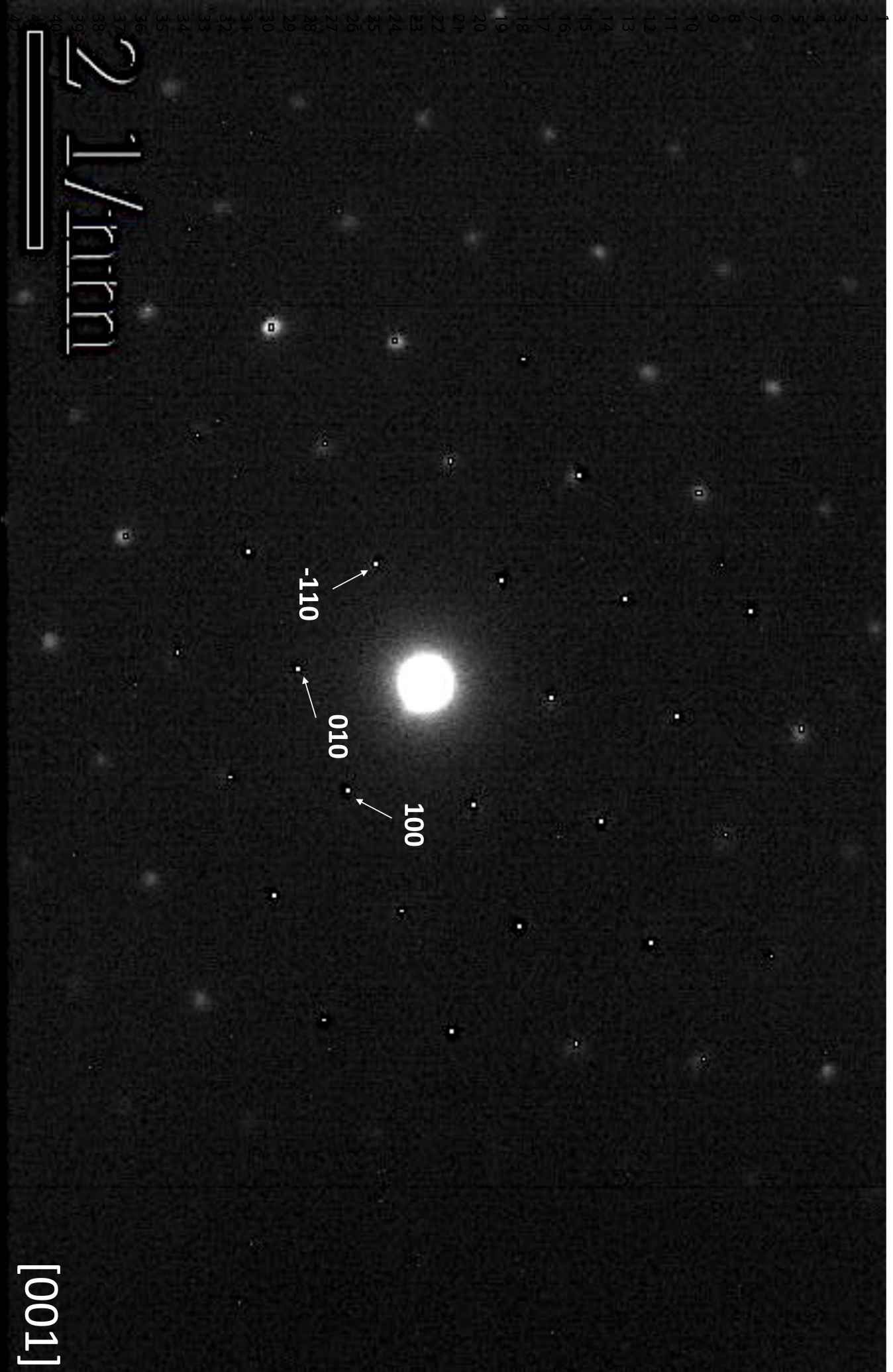
days

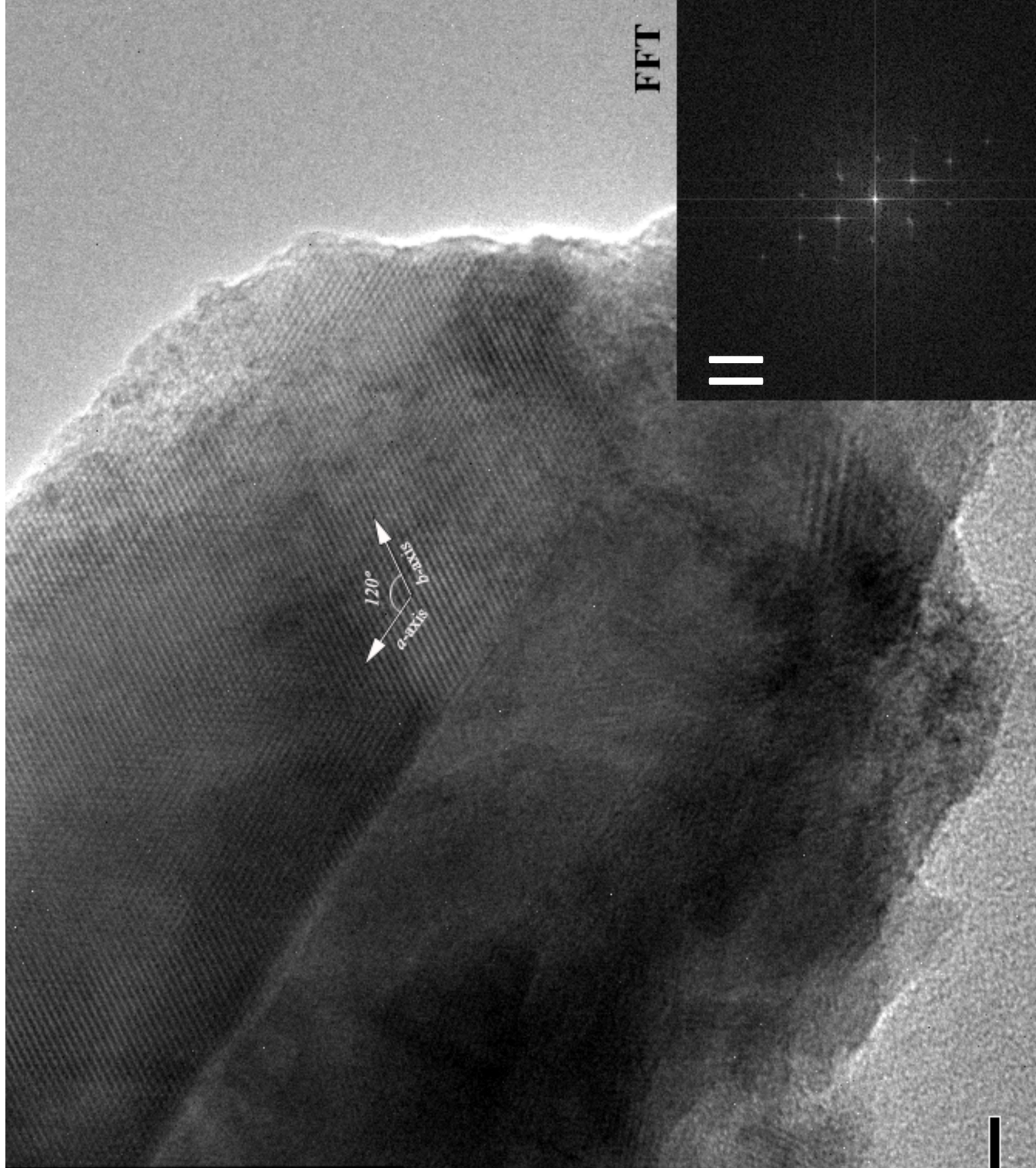
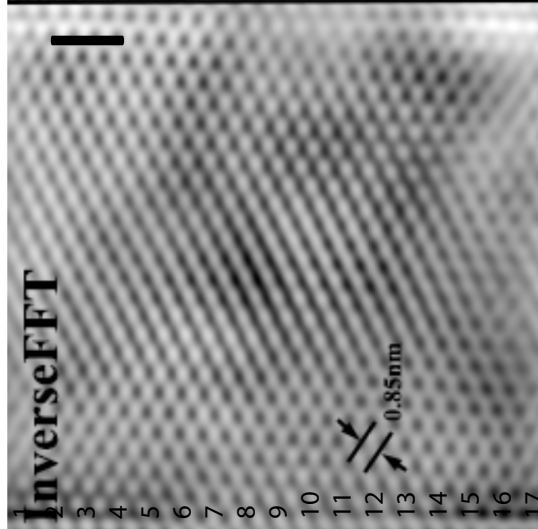


1 2 3 4 5 6 7 8 9 10 11 12 13 14 15 16 17 18 19 20 21 22 23 24 25 26 27 28 29 30 31 32 33 34 35 36 37 38 39 40 41 42 43 44 45 46 47

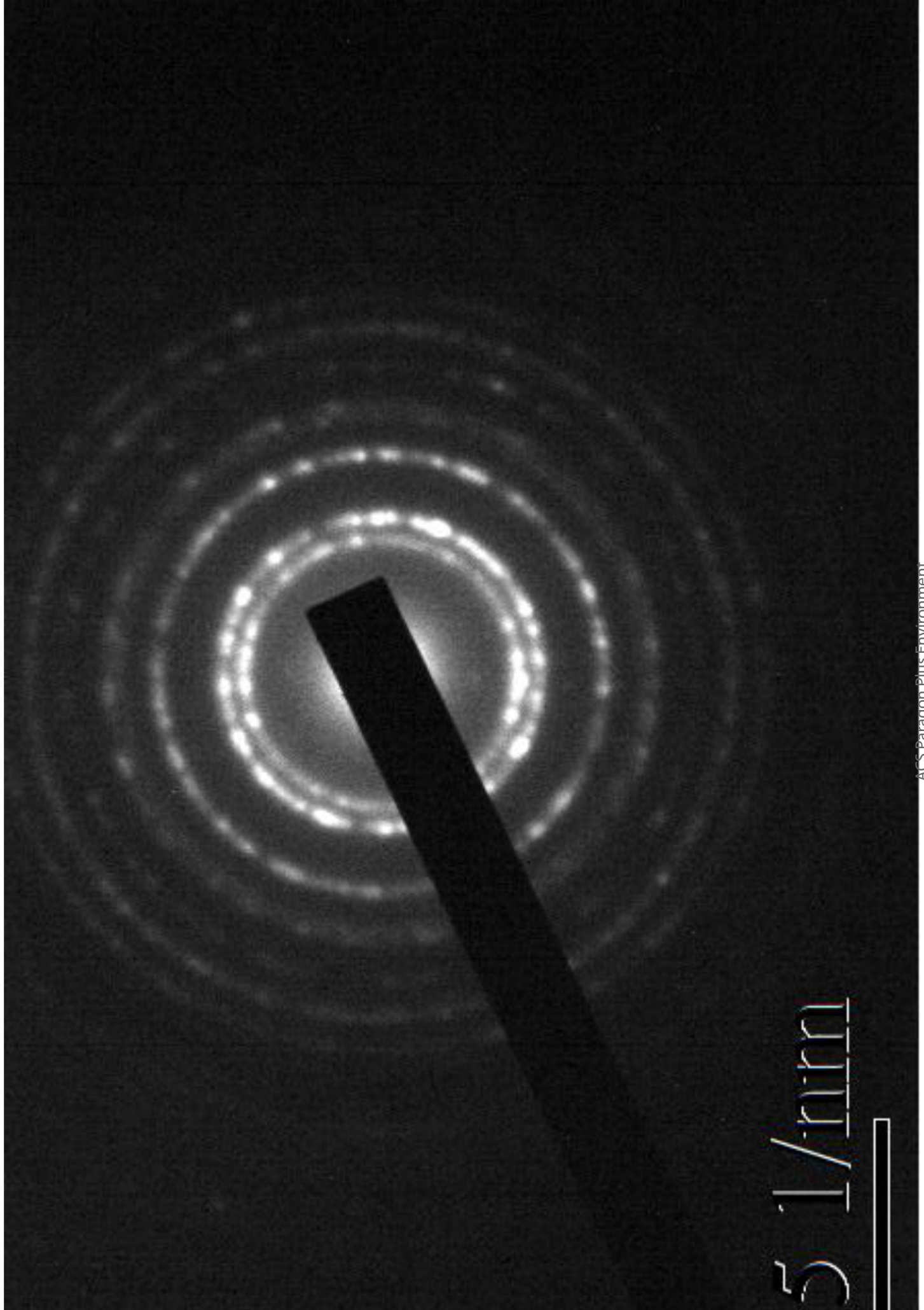




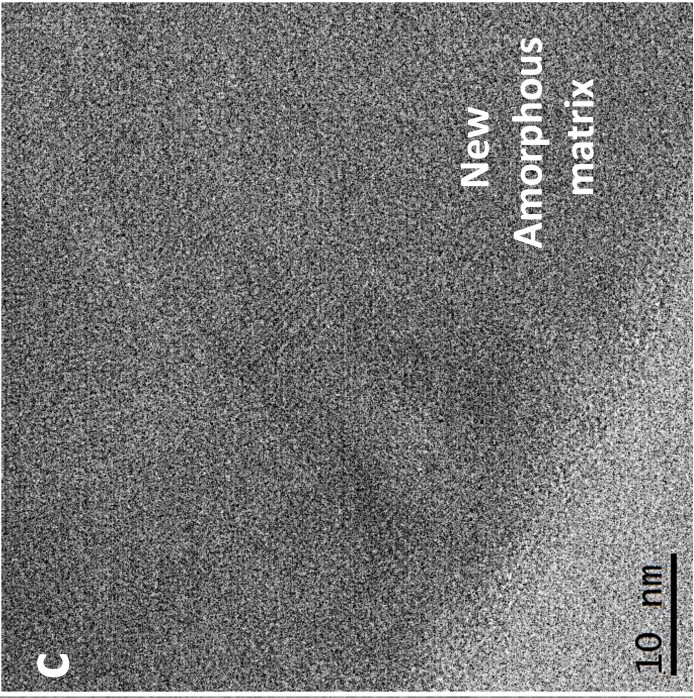
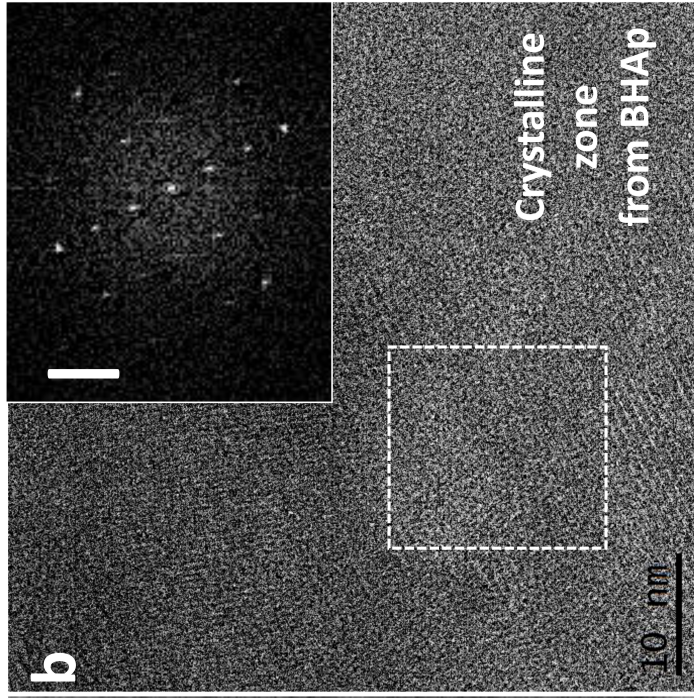
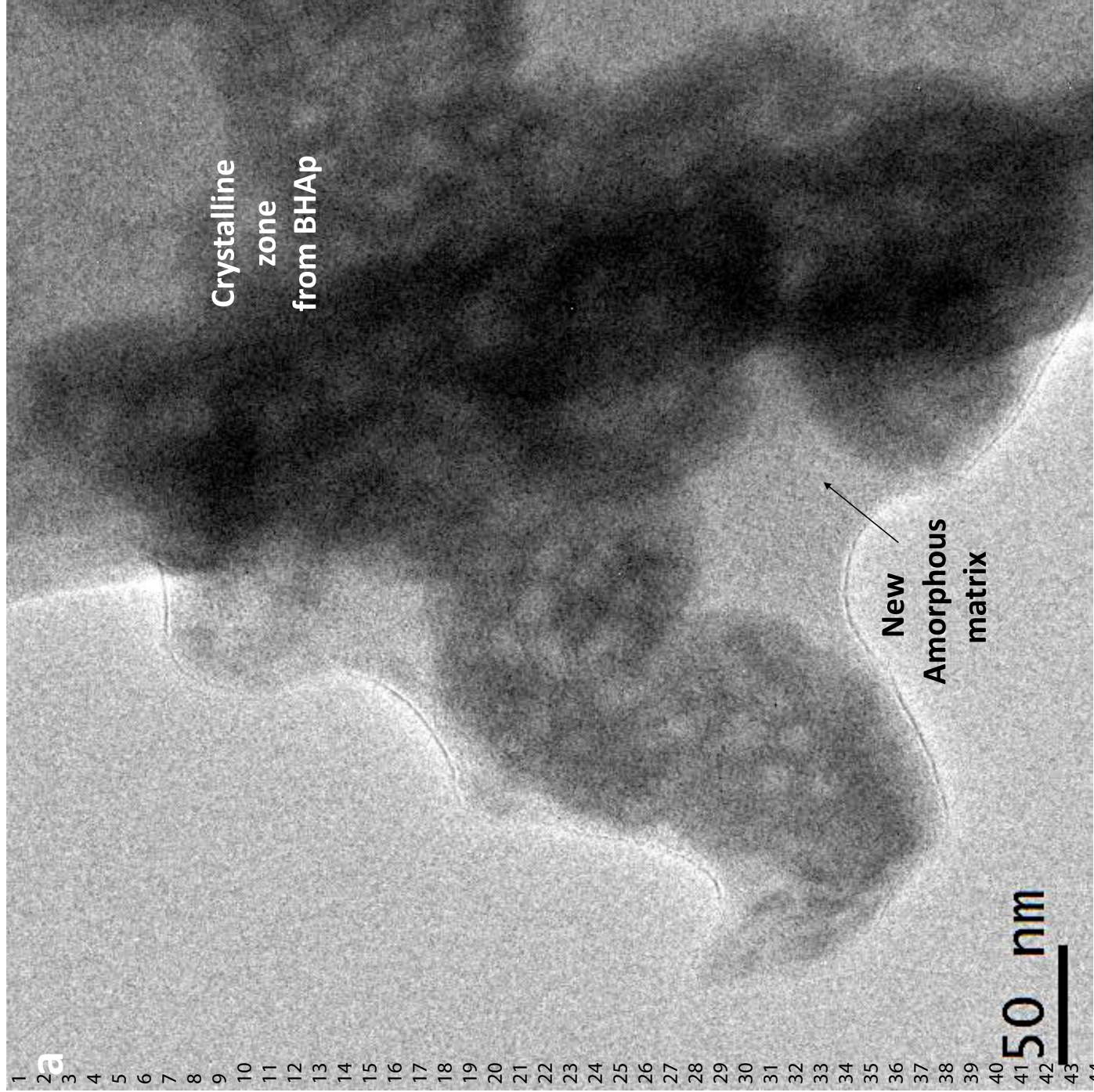


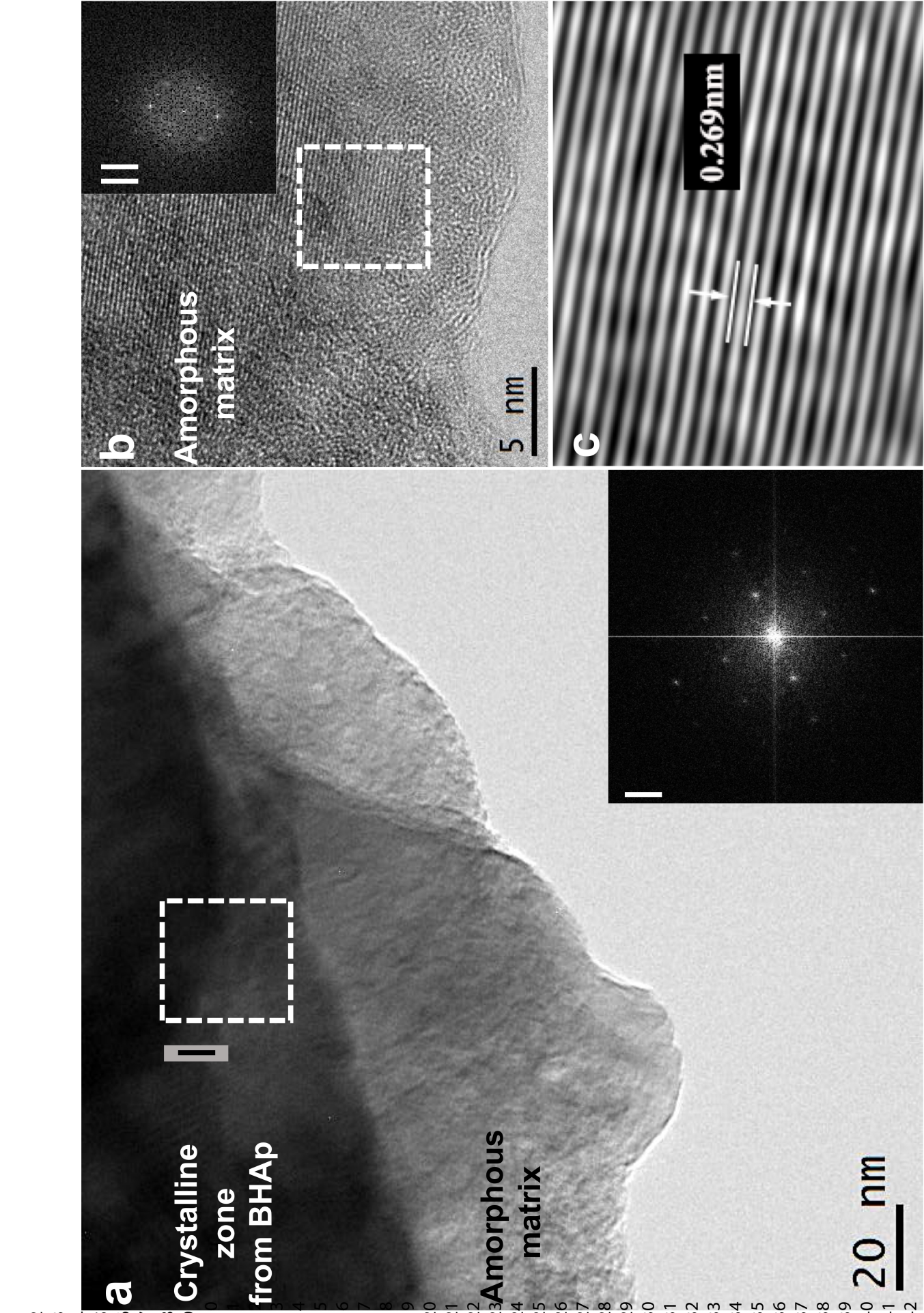


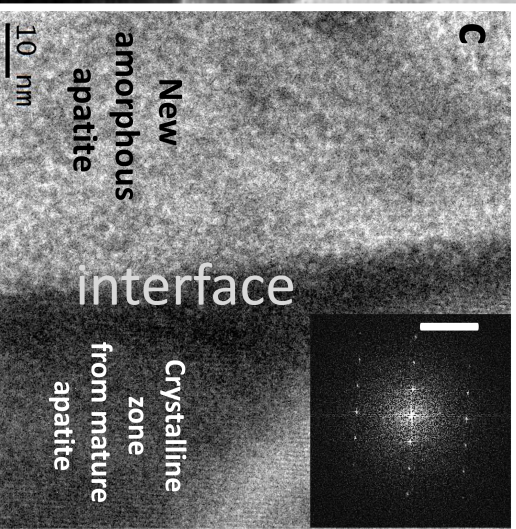
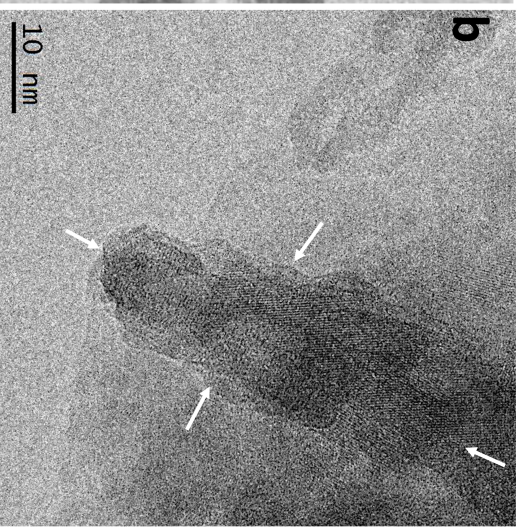
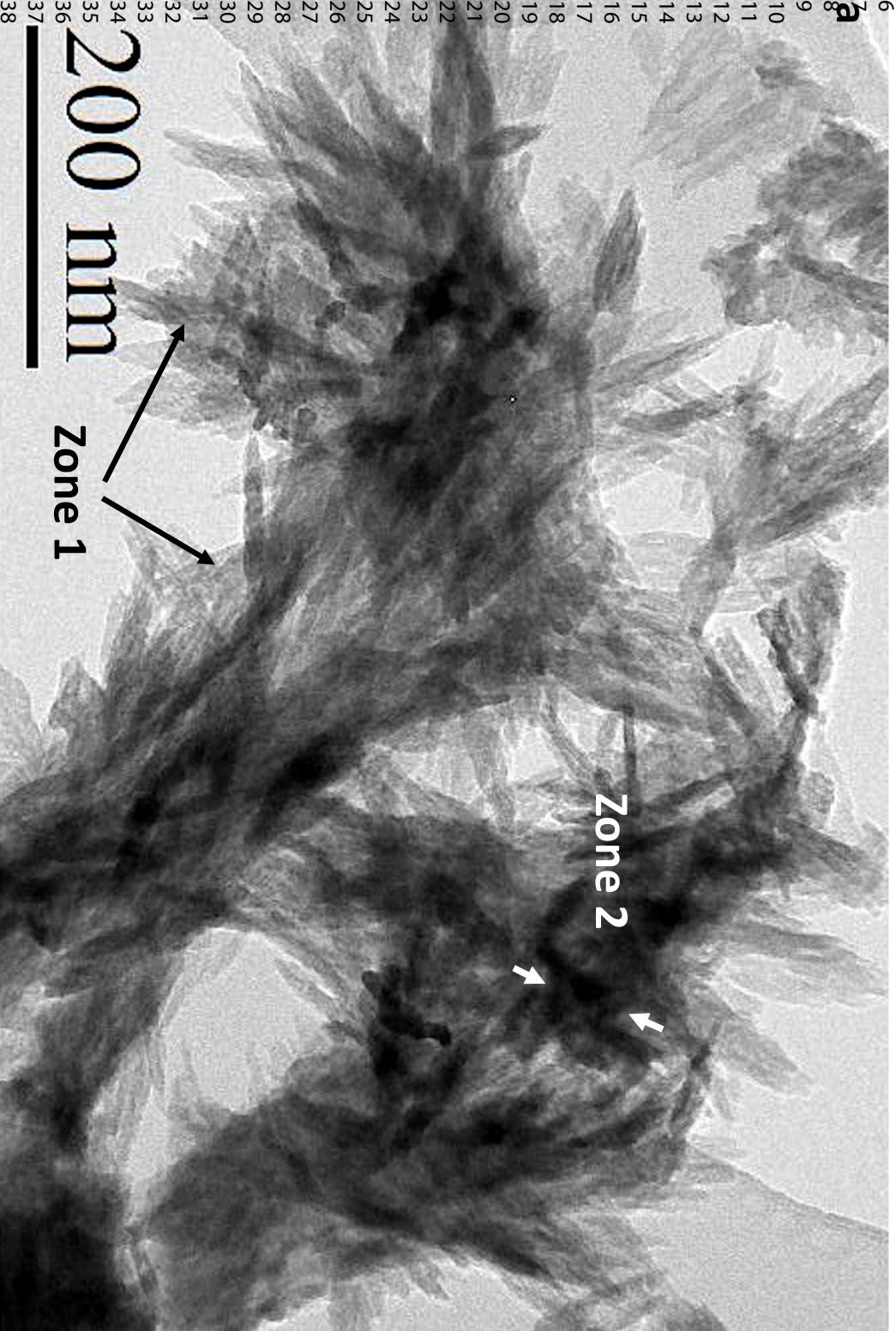
1
2
3
4
5
6
7
8
9
10
11
12
13
14
15
16
17
18
19
20
21
22
23
24
25
26
27
28
29
30
31
32
33
34
35
36
37
38
39
40
41
42
43
44



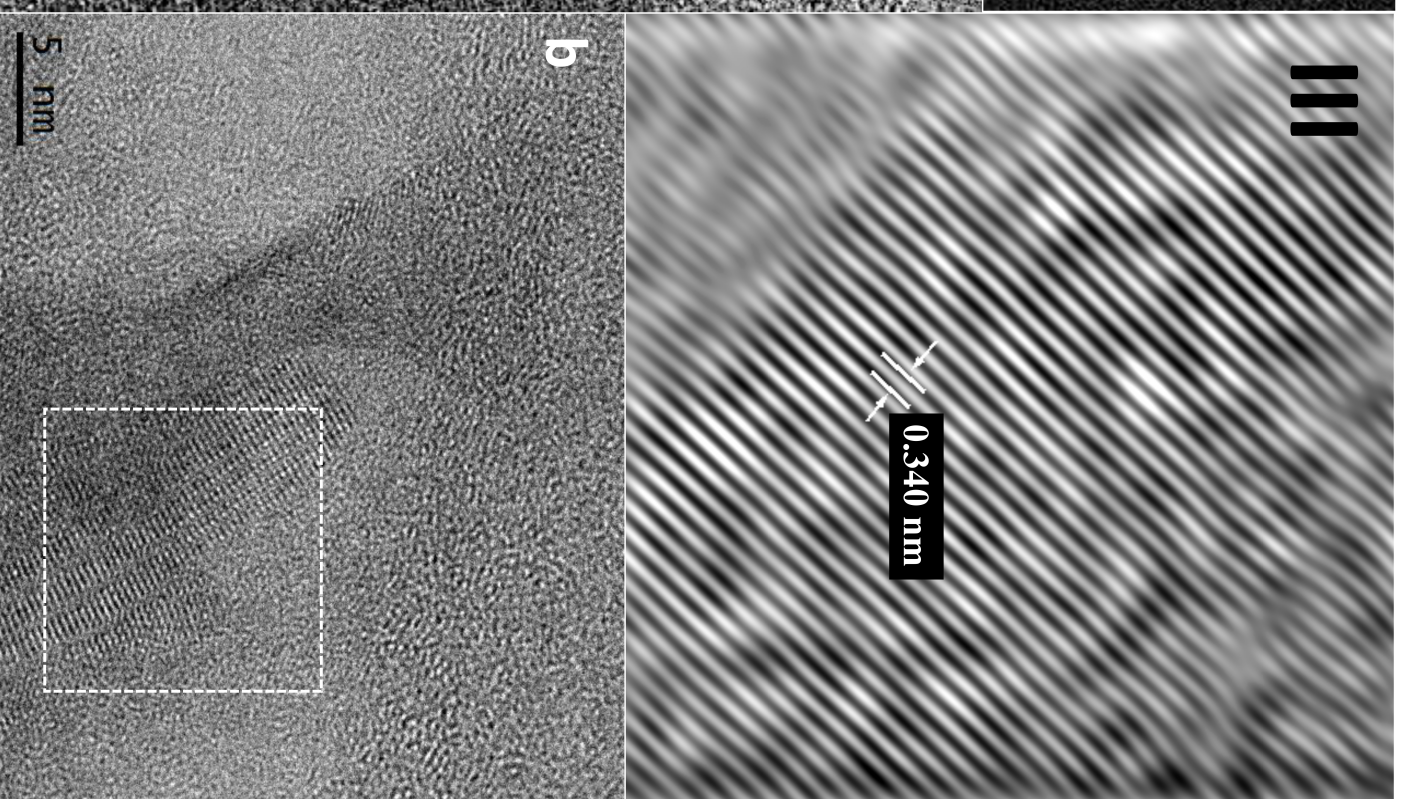
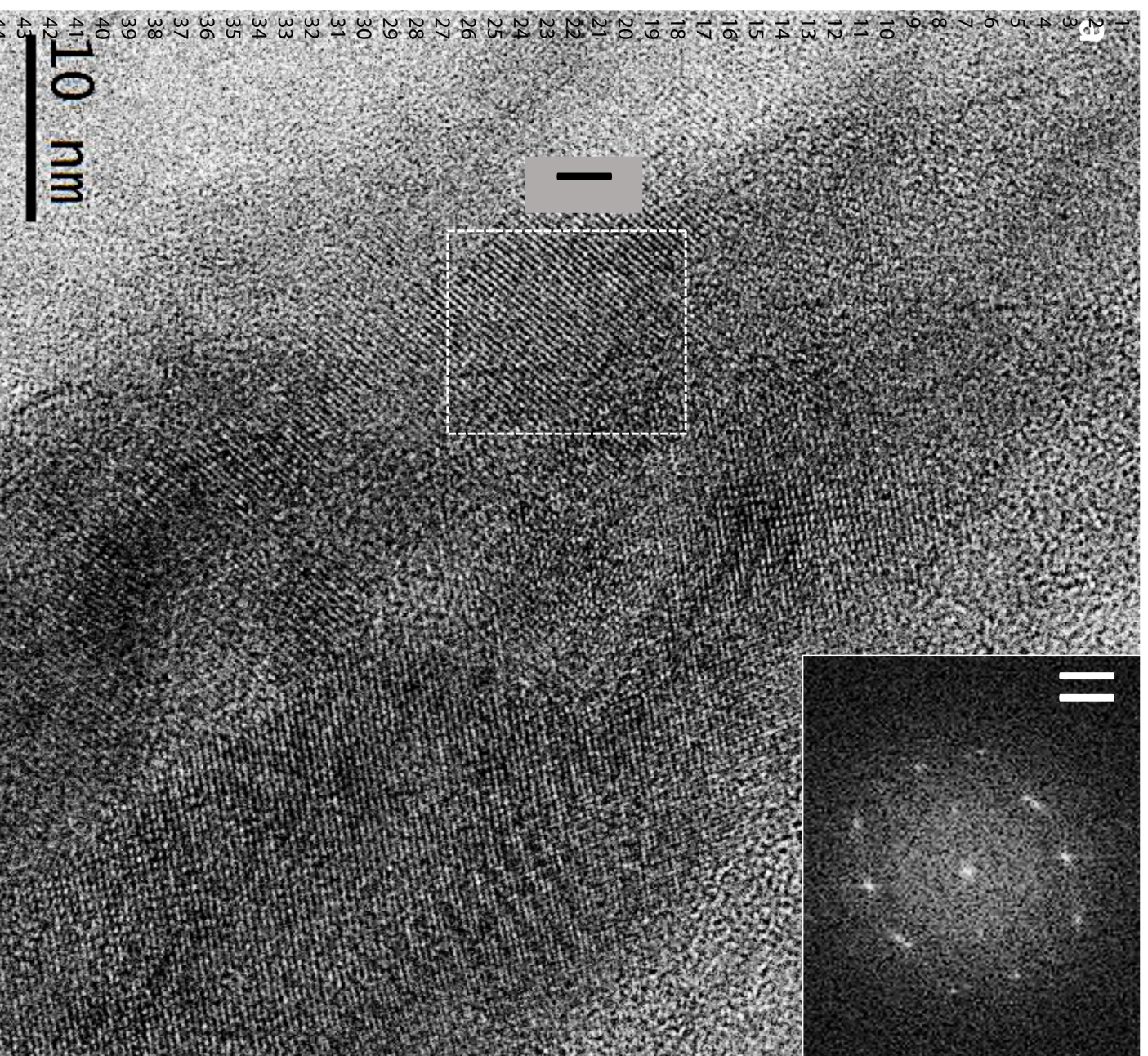
45
46
47

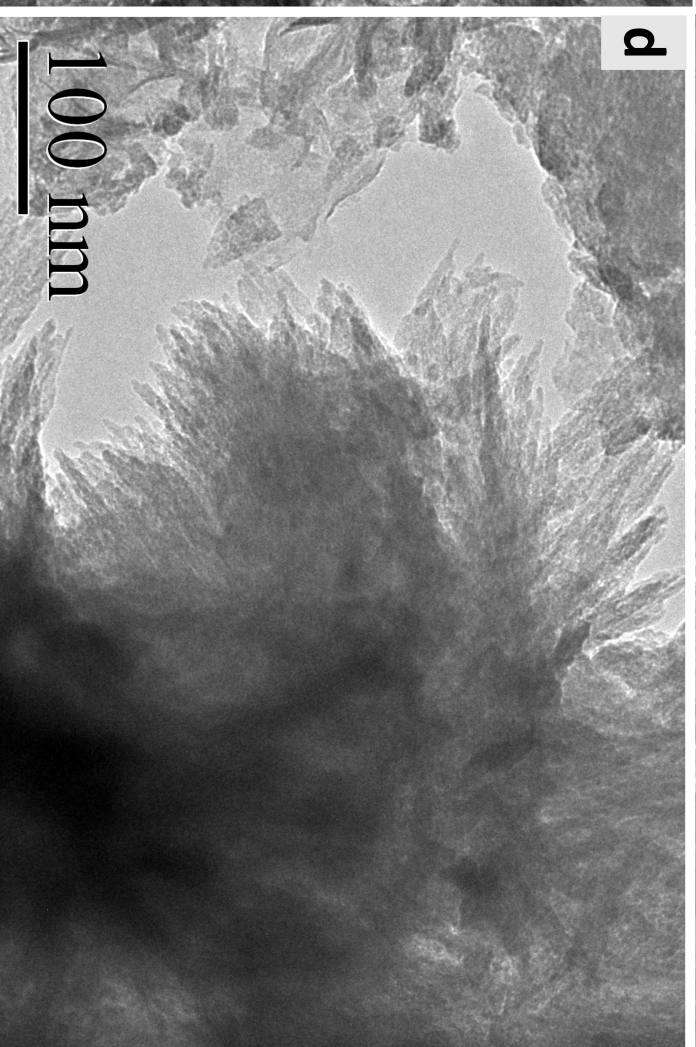
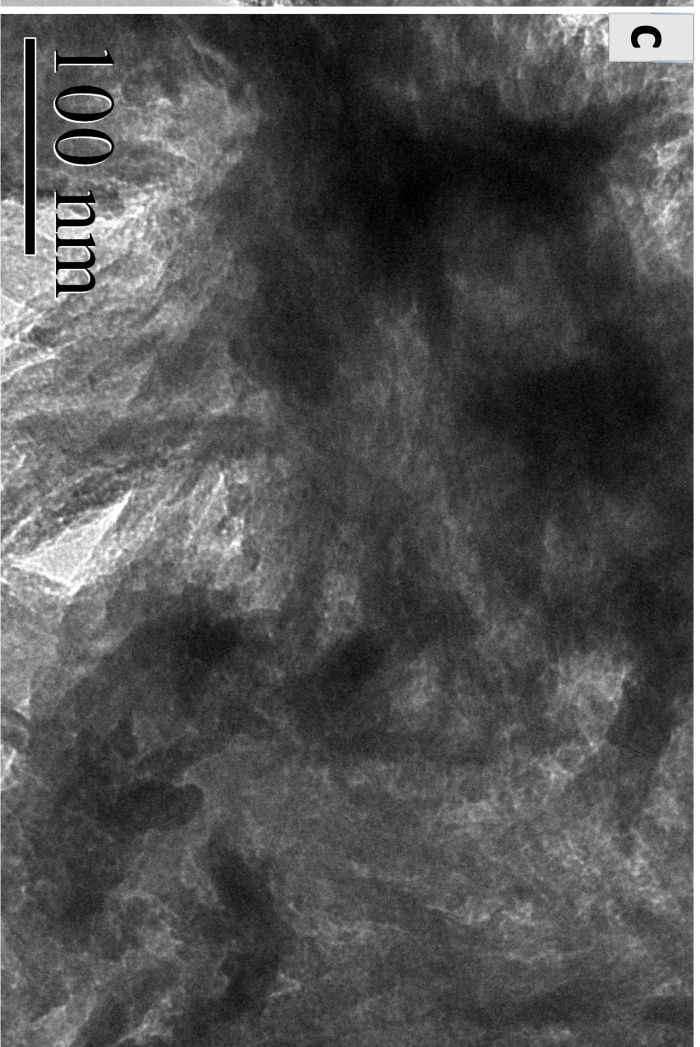
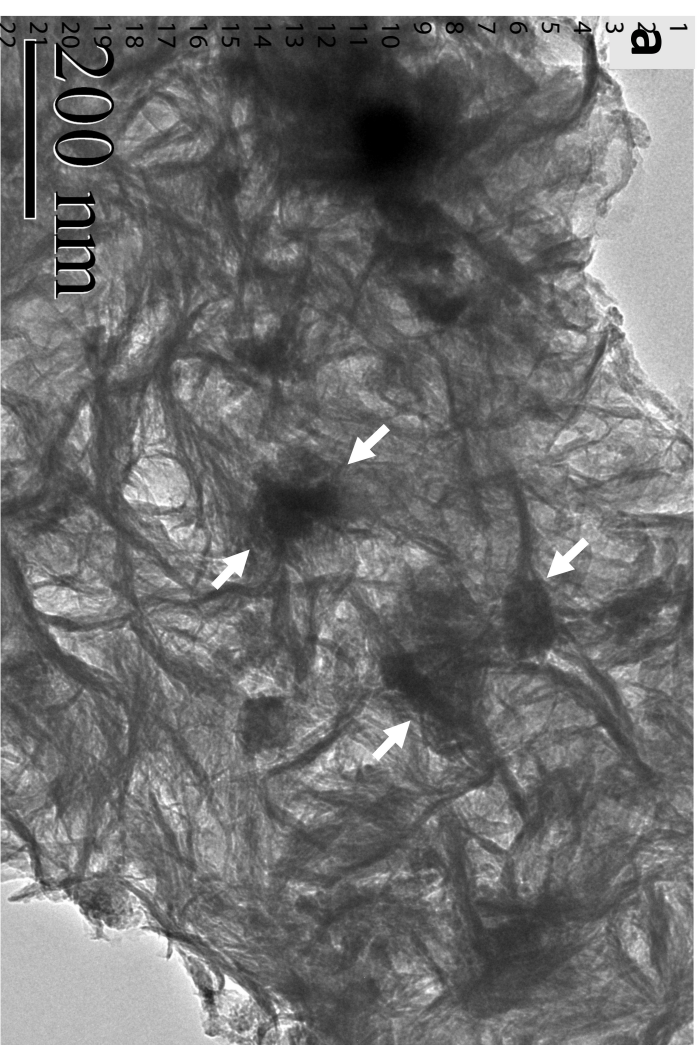




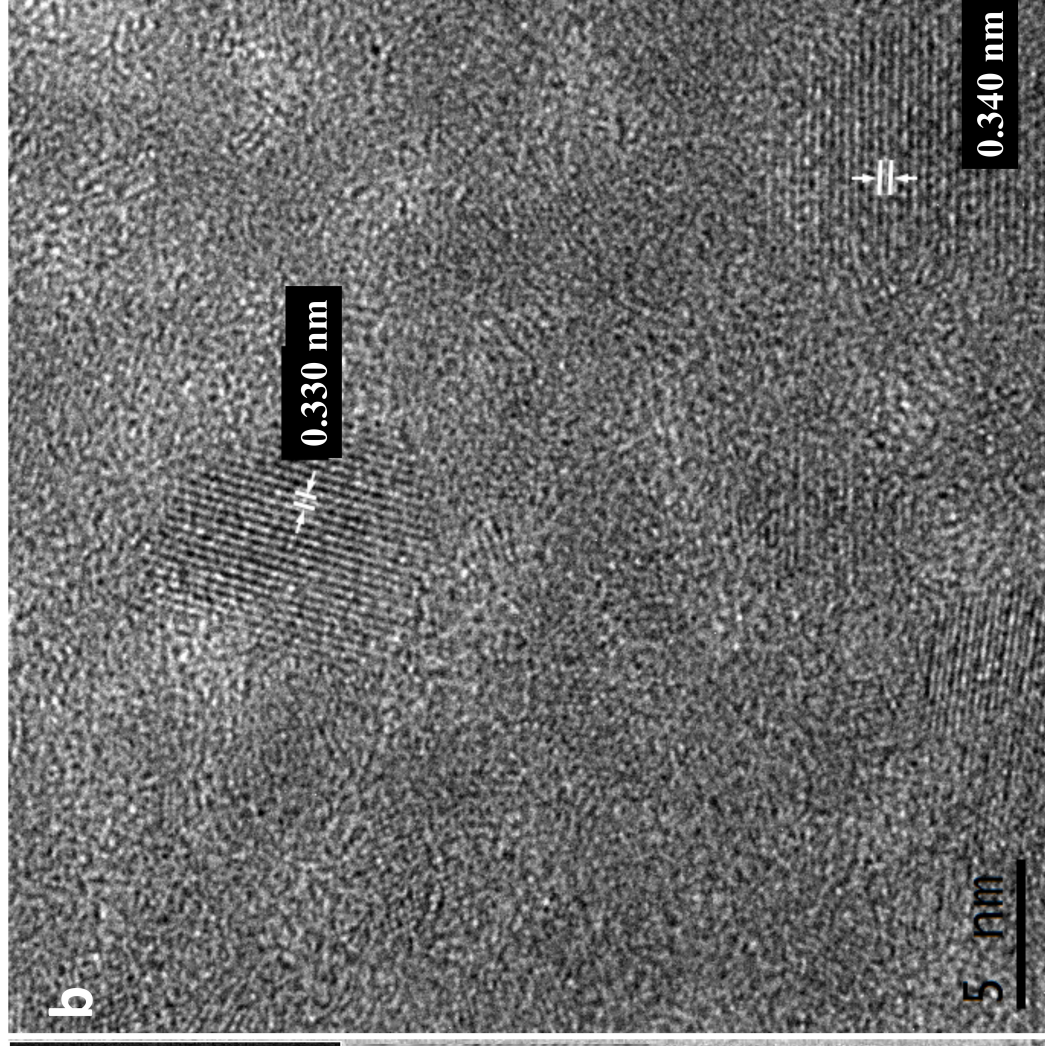
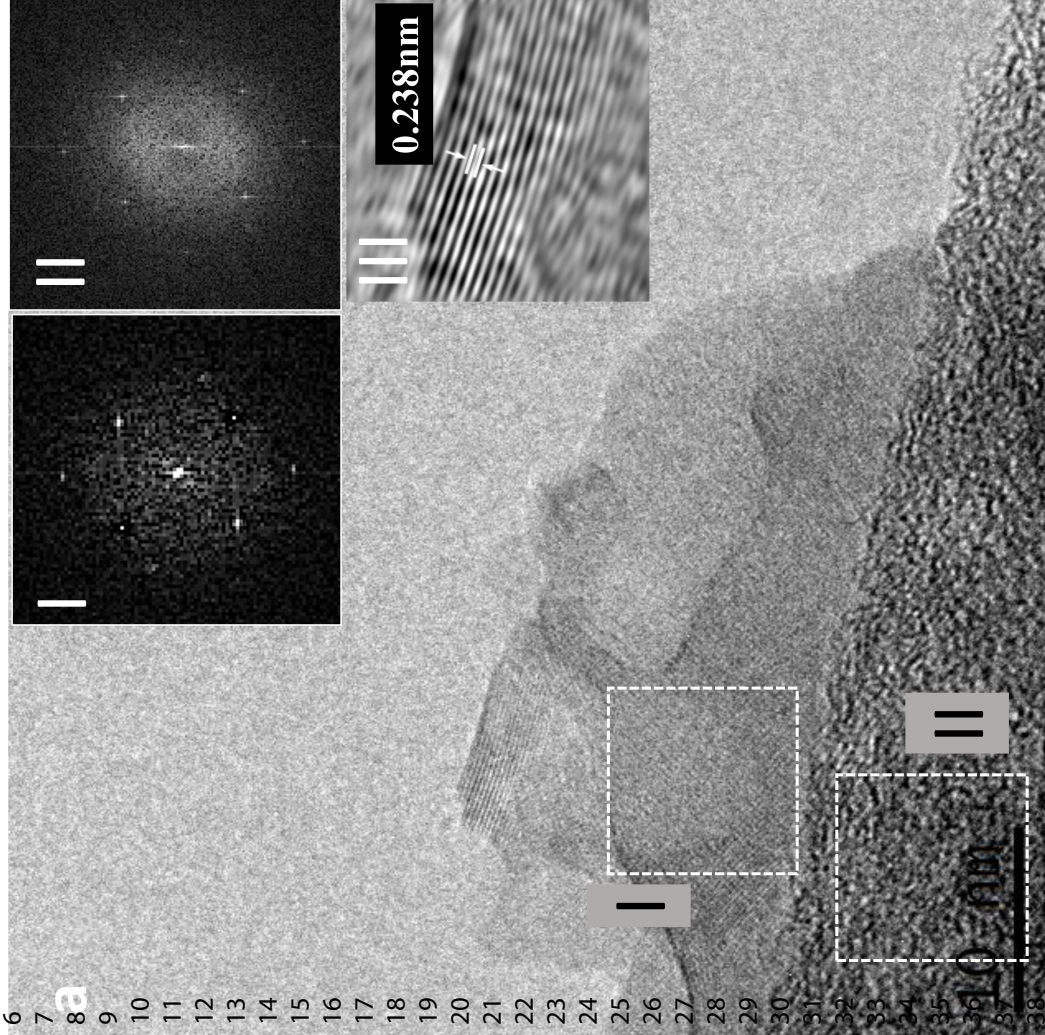


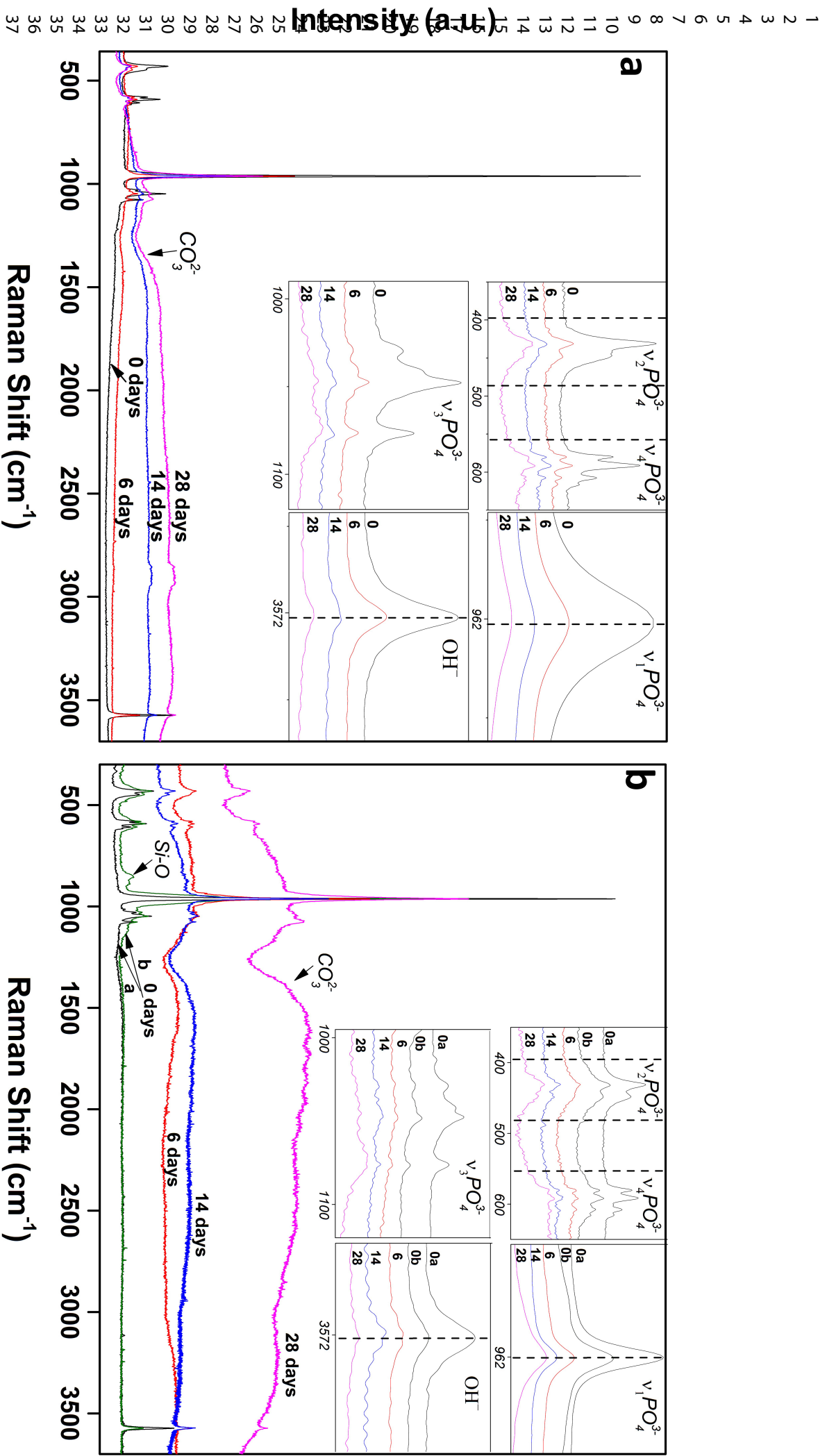
1
2
3
4
5
6
7
8
9
10
11
12
13
14
15
16
17
18
19
20
21
22
23
24
25
26
27
28
29
30
31
32
33
34
35
36
37
38
39
40
41
42
43
44
45
46
47





1
2
3
4
5
6
7
8
9
10
11
12
13
14
15
16
17
18
19
20
21
22
23
24
25
26
27
28
29
30
31
32
33
34
35
36
37
38
39
40
41
42
43
44
45
46
47





Sample	Days	Phase	% wt. Phase	<i>a</i> (Å)	% <i>a</i> strain	<i>c</i> (Å)	% <i>c</i> strain	Crystallite size (Å)	Volume (Å ³)	Ca/P	χ^2	<i>R_f</i>
	0	HAp	100	9.419	0.137	6.886	-0.077	2718.785	529.093	1.643	1.622	0.059
	6	HAp	100	9.422	0.111	6.884	-0.038	285.663	529.828	1.730	2.140	0.059
BHAp	14	HAp	100	9.439	-0.074	6.877	0.065	367.604	528.688	1.727	1.606	0.072
	28	HAp	100	9.429	0.027	6.887	-0.085	403.468	530.302	1.770	1.804	0.049
		HAp	67.26	9.418	0.147	6.887	-0.093	3477.474	529.073	1.553		
	0	Nagel	32.74	10.673	-0.370	21.644	-0.008	1389.105	2135.075		1.270	0.041
		HAp	71.856	9.415	0.179	6.887	-0.083	1987.066	528.687	1.398		
23BHAp/ Nagel composite	6	Nagel	28.144	10.652	-0.173	21.625	0.079	205.120	2135.078		1.295	0.052
	14	HAp	72.151	9.427	0.048	6.887	-0.090	447.238	530.104	1.889	1.407	0.061
		Nagel	27.849	10.531	0.965	22.011	-1.704	152.834	2113.865			
	28	HAp	100	9.424	0.083	6.885	-0.059	417.439	529.579	1.736	1.358	0.070

χ^2 : Goodness coefficient ***R_f*** : Structure factor

Assignment	Stoichiometric HAp [66,67]	Carbonate HAp Type B [66,67]	BHAP				BHAp/Nagel composite			
			0 days	6 days	14 days	28 days	0 days	6 days	14 days	28 days
$\nu_1\text{PO}_4^{3-}$	964	961	962.28	962.26	962.37	962	962.06 (a)	962.14	961.99	962.09
							962.31 (b)			
$\nu_2\text{PO}_4^{3-}$	433	432	430	431	431	431	431	437	430	437
	448	445	440	448	446	446	448		448	
									488	
$\nu_3\text{PO}_4^{3-}$	1029	1026	1029	1029	1029	1029	1029			1037
	1034									
	1041		1041	1041	1042	1046	1042			
	1048	1047	1047	1047	1048		1048	1049		
	1057									
	1064									
$\nu_4\text{PO}_4^{3-}$	1077	1070	1076	1076	1077	1073	1076			1070
				573						
	580	579	579	580		580	580	580	580	
	591	590	591	591		592	591	590	590	
	607	609	607	607		607	607	609	609	
	614		628	615		615		615	615	
OH-	3573		3572.97	3592.8	3572.26	3572.25	3572.75	3572.1	3572.1	3572.47
							853 (b)			
Si-O							886 (b)			
$\nu_1\text{CO}_3^{2-}$	1070					1073			1070	

Ions concentration [ppm]	Sample			Reported values [19,52,68,69]		
	Control	BHAp	BHAp/Nagel composite	Positive individual effect	Positive combinatory effect	Cytotoxic
[Si]	0.14 ± 0.01	1.06 ± 0.00	9.59 ± 0.02	<20	<33.36	>170
[Ca]	0.51 ± 0.12	39.95 ± 1.49	81.34 ± 3.23	<320	<104.69	>400
[Mg]	0.17 ± 0.04	10.15 ± 0.12	10.49 ± 0.10	<24	<13.13	>35
[P]	0.71 ± 0.19	13.07 ± 2.38	6.06 ± 0.00	-	-	-
[Na]	5.65 ± 0.38	25.42 ± 1.62	65.16 ± 2.94	-	-	-